Regulation of neuronal input transformations by tunable dendritic inhibition

Matthew Lovett-Barron[1], Gergely F Turi[1], Patrick Kaifosh[1], Peter H Lee[2], Frédéric Bolze[3], Xiao-Hua Sun[3], Jean-François Nicoud[3], Boris V Zemelman[4], Scott M Sternson[2] & Attila Losonczy[1]

Transforming synaptic input into action potential output is a fundamental function of neurons. The pattern of action potential output from principal cells of the mammalian hippocampus encodes spatial and nonspatial information, but the cellular and circuit mechanisms by which neurons transform their synaptic input into a given output are unknown. Using a combination of optical activation and cell type–specific pharmacogenetic silencing *in vitro*, we found that dendritic inhibition is the primary regulator of input-output transformations in mouse hippocampal CA1 pyramidal cells, and acts by gating the dendritic electrogenesis driving burst spiking. Dendrite-targeting interneurons are themselves modulated by interneurons targeting pyramidal cell somata, providing a synaptic substrate for tuning pyramidal cell output through interactions in the local inhibitory network. These results provide evidence for a division of labor in cortical circuits, where distinct computational functions are implemented by subtypes of local inhibitory neurons.

The output of principal cells in the hippocampus can range from silence to high-frequency bursts of action potentials[1,2]. The spatial map theory of the hippocampus posits that sparse coding for the cognitive representation of space is implemented by a subset of principal neurons that display location-specific firing during navigation, whereas other neurons remain silent[3,4]. The mechanisms by which the hippocampal circuit transforms synaptic input into spike output conducive to this sparse coding scheme remain controversial[5,6]. Spatiotemporal pattern-dependent integration of excitatory inputs can generate distinct spike outputs by promoting linear or supralinear integration schemes in dendrites[7–10], and could potentially provide mechanisms for firing behaviors observed in pyramidal cells of the hippocampal CA1 region (CA1PCs) *in vivo*[11,12]. Active dendritic electrogenesis and the all-or-none properties of axonal spiking, however, yield a limited dynamic range of input processing because firing rates saturate even at relatively low levels of input. This bistable network behavior constrains the capacity for neural coding, suggesting a requirement for multimodal circuit processing[5,13].

One candidate for such processing is the diverse population of local GABA-releasing (GABAergic) cells in CA1, which inhibit pyramidal cells along their entire somatodendritic axis through distinct perisomatic- and dendrite-targeting GABAergic circuits[14–16]. The influence of perisomatic inhibition on pyramidal cells has been well documented, with GABA release from basket and axo-axonic cells acting to control spike timing and oscillatory activity[17–19]. However, CA1PCs receive the vast majority of their inhibitory inputs at their dendrites[20,21] and the activity of dendrite-targeting interneurons coincides with the activity of presynaptic excitatory inputs *in vivo*[16,21,22]. This raises the possibility that dendritic inhibition serves to regulate local excitatory input processing[8,23,24], which could be particularly important given the active properties of CA1PC dendrites. Indeed, inhibition has been shown to be involved in controlling both Ca^{2+} spikes in the apical trunk[25] and NMDA receptor (NMDAR) activation[26] in thin dendrites of hippocampal pyramidal neurons. The presence or absence of dendritic inhibition in CA1 could contribute to defining the spike output of CA1PCs to synaptic excitation in a given environment. However, the causal role of identified dendritic inhibitory circuits in neuronal input-output transformations remains unknown, as there have been difficulties in achieving precise experimental control over distinct excitatory and inhibitory circuit elements. We used a panel of photoactivation and cell type–specific optogenetic and pharmacogenetic techniques to control distinct components of excitation and inhibition in the hippocampal CA1 circuit *in vitro*, and assessed the function of dendritic inhibition in CA1PC input-output transformations.

RESULTS

Inhibition of dendritic integration in single branches

Previous work has established the individual dendritic branch as a basic unit of excitatory synaptic integration in pyramidal cells[10,27–29]. Thus, we first sought to examine whether the influence of inhibition on input-output transformations in single dendritic branches of CA1PCs depends on the subcellular location of GABAergic conductance. We used multi-site two-photon glutamate uncaging[10] to deliver excitatory inputs to distal parts of single radial oblique or basal dendrites of CA1PCs ($141 \pm 6 \, \mu m$ distal to soma, $n = 11$; **Fig. 1a** and Online Methods) in acute slices of mouse hippocampus and recorded the resulting subthreshold depolarization with somatic whole-cell recordings.

[1]Department of Neuroscience, Columbia University, New York, New York, USA. [2]Howard Hughes Medical Institute, Janelia Farm Research Campus, Ashburn, Virginia, USA. [3]Laboratoire de Biophotonique et Pharmacologie UMR 7213 Centre National de la Recherche Scientifique/Université de Strasbourg, Strasbourg, France. [4]Center for Learning and Memory, University of Texas at Austin, Austin, Texas, USA. Correspondence should be addressed to A.L. (al2856@columbia.edu).

Figure 1 Location-specific inhibition shapes excitatory synaptic integration in single CA1PC dendrites. (**a**) Two-photon image stack of recorded hippocampal CA1PC (green) and locations of two-photon glutamate uncaging and one-photon GABA uncaging. Inset, selected dendrite with 40 glutamate uncaging spots. (**b**) Somatic membrane potential responses and subthreshold input-output curve for a single dendritic branch to increasing number of stimulated synapses (top, 7, 17, 27, 32, 38 and 40 spines) without inhibition (somatic spikes truncated) and in the presence of dendritic or somatic inhibition. (**c**) Summary of the differences in single-branch input-output functions according to the position of inhibition (expected peak depolarization: arithmetic sum of isolated single-spine excitatory postsynaptic potentials, EPSPs). Solid lines in **b** and **c** are sigmoidal fits to the data used to calculate gain changes. Error bars indicate ± s.e.m.
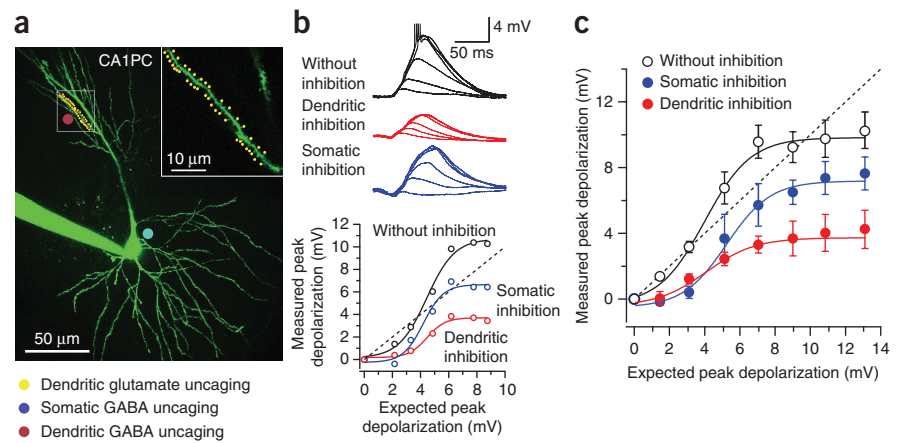
To assess the influence of inhibition on this single branch input-output relationship, we paired dendritic excitation with one-photon GABA uncaging[30] colocalized with excitatory inputs on the dendritic branch or located at the soma (**Fig. 1** and **Supplementary Fig. 1**). We found that inhibitory postsynaptic conductance (IPSG) colocalized with excitation (measured at the soma, 2.3 ± 0.2 nS, $n = 11$) was more effective at shunting nonlinear dendritic depolarizations, which are dependent on Na^+ channels and NMDARs[10,26,28], and markedly suppressed the branch input-output function to the sublinear range (Δgain/gain = $64 \pm 4\%$, $n = 11$). This effect was location dependent, as inhibition localized at the soma (IPSG = 4.3 ± 1 nS, $n = 8$) only moderately affected the slope of the branch input-output relationship (Δgain/gain = $21 \pm 4\%$, $n = 8$; **Fig. 1b,c**). These data indicate that the effective spatial compartmentalization of conductance along the somatodendritic membrane surface of pyramidal neurons[31,32] is reflected in location-dependent effects of inhibition on input-output transformations in single dendritic branches of CA1PCs.

Manipulating excitatory and inhibitory circuitry in CA1

In the engaged hippocampal network, CA1PCs are driven by excitatory synaptic inputs that are distributed over multiple branches of their dendritic arborizations, and inhibition exerts its effects with GABAergic interneurons recruited through synaptic excitation. To determine whether the observed subcellular location dependence of inhibition persists under more realistic input conditions, we devised a strategy to activate the CA1 circuit *in vitro* with photostimulation of the excitatory CA3 Schaffer collaterals (CA3SCs) and subsequently silence genetically designated populations of local interneurons to assess their function.

We bilaterally injected a recombinant adeno-associated virus (rAAV) into dorsal CA3 of adult mice to induce Channelrhodopsin-2 (ChR2) expression in CA3SC axons, located in strata radiatum and oriens of CA1 (rAAV:*ChR2-sfGFP*; **Fig. 2a** and Online Methods). Grid photostimulation of the CA3SCs, the numerically largest source of excitatory input to CA1 (ref. 5), drove pyramidal cells and interneurons in the CA1 circuit *in vitro* with phasic excitatory synaptic input. We determined the suprathreshold input-output transformation by systematically varying the intensity of CA3SC photostimulation and measuring the firing rate output of CA1PCs with whole-cell recordings from the soma. We quantified photostimulation intensities in terms of mean excitatory currents (I_{Esyn}) measured in CA1PCs under $GABA_A$ receptor ($GABA_A R$) blockade (20 µM gabazine; **Fig. 2b**),

a direct measure of CA3SC input because of the low levels of recurrent excitatory connectivity present in CA1 (ref. 33). Grid photostimulation produced a spatially disperse activation of CA3SC axons, comparable to estimates of CA3SC inputs during theta exploratory states *in vivo*[5,34] (see Online Methods). CA3SC photostimulation effectively recruited polysynaptic GABAergic inhibition that strongly counteracted excitation, resulting in low CA1PC firing rates even for relatively high levels of excitatory input. Following pharmacological blockade of $GABA_A Rs$, CA1PCs greatly increased their firing rates (maximum firing rate: control, 18.2 ± 3.9 Hz; gabazine, 81 ± 9 Hz, $n = 27$; **Fig. 2c,d**).

To selectively and completely inhibit defined populations of highly active GABAergic neurons, we required a genetically encoded neuronal silencing system that could be acutely engaged and strongly suppresses neuronal activity. For this, we employed a chimeric ligand-gated ion channel ($PSAM^{L141F}$-GlyR)[35] that could be targeted exclusively to genetically defined subpopulations of GABAergic interneurons in CA1 (ref. 36). Application of its small-molecule agonist ($PSEM^{308}$) results in rapid silencing of $PSAM^{L141F}$-GlyR$^+$ cells though the activation of a shunting Cl^- conductance[35]. We verified this approach using conditional viral expression of $PSAM^{L141F}$-GlyR nonselectively in local GABAergic interneurons to achieve complete pharmacological blockade of inhibition in CA1. For this, we injected rAAVs into the dorsal hippocampi of *Gad65* (also known as *Gad2*)-*cre* mice[19] (rAAV:*ChR2-sfGFP* into CA3; rAAV($PSAM^{L141F}$-*GlyR*)^{Cre} and rAAV(*tdTomato*)^{Cre} into CA1), driving robust expression of ChR2-sfGFP in the CA3SCs, and $PSAM^{L141F}$-GlyR/tdTomato in GAD65$^+$ local inhibitory neurons (labeling efficiency = $78 \pm 5\%$, $n = 8$; **Fig. 2e**, **Supplementary Fig. 2a–c** and Online Methods). Bath application of $PSEM^{308}$ completely silenced recorded $PSAM^{L141F}$-GlyR$^+$ interneurons in all cases (3 µM, $n = 18$), with no spikes being elicited by somatic current injection or maximal phasic CA3SC photostimulation (**Fig. 2f,g**), and without affecting the intrinsic properties of $PSAM^{L141F}$-GlyR cells (interneurons, $n = 16$; CA1PCs, $n = 30$; **Supplementary Fig. 2d–f**). Closely mimicking the effects of blocking $GABA_A Rs$ pharmacologically, pharmacogenetic silencing of GAD65$^+$ interneurons increased the firing rate of CA1PCs to CA3SC photostimulation (maximum firing in $PSEM^{308}$ = 67 ± 8 Hz, $n = 6$; **Fig. 2h,i**). Together, these results revealed a major divisive and moderate subtractive influence of local GABAergic neurons on the CA1PC input-output relationship (Δgain/gain: $PSEM^{308}$, $677 \pm 150\%$, $n = 6$; gabazine, $732 \pm 85\%$, $n = 22$; offset: $PSEM^{308}$, 79 ± 19 pA; gabazine,
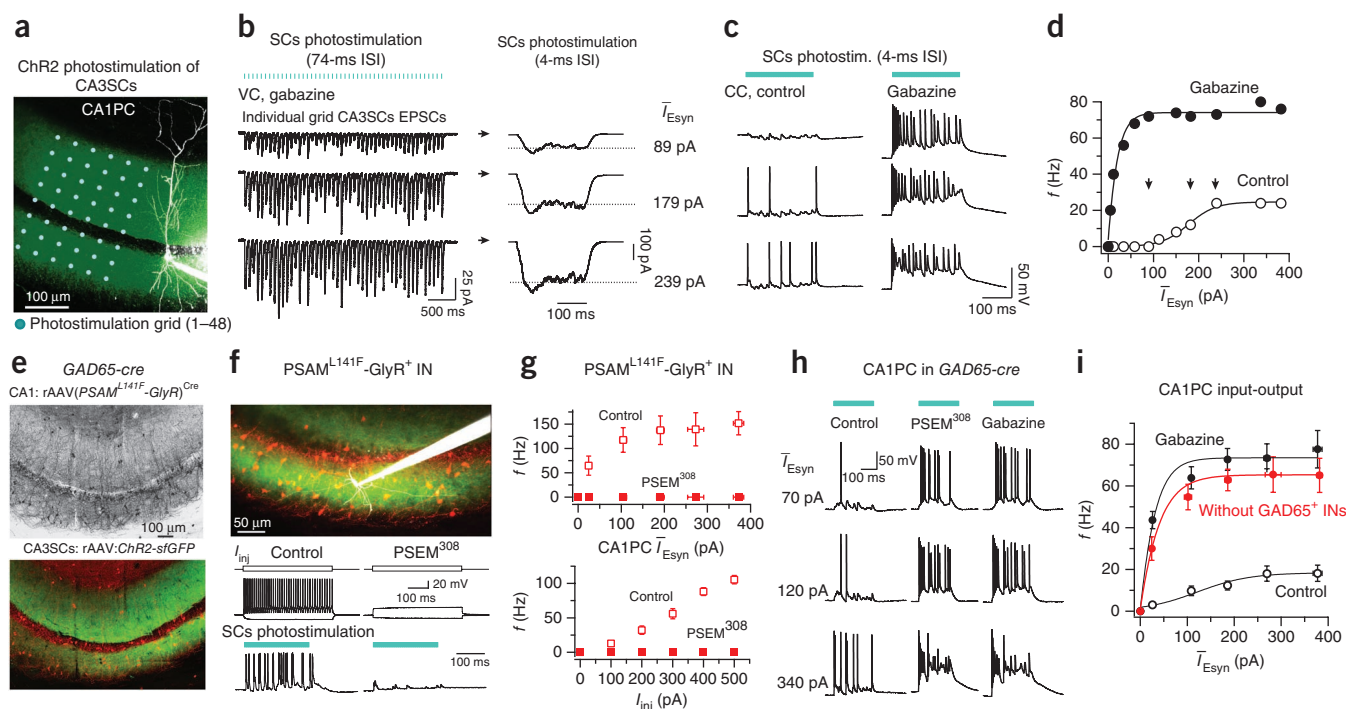
Figure 2 Independent control over excitatory and inhibitory synaptic inputs to CA1PCs. (**a**) Two-photon stack of recorded CA1PC (white), ChR2-sfGFP+ CA3SCs (green), and the 6 × 8–point photostimulation grid. (**b**) Voltage-clamp recordings (VC) of excitatory inputs evoked from each of the 48 points in the CA3SC photostimulation grid at three levels of laser intensity (left, 74-ms interstimulus interval, ISI). Individual input currents were used to calculate the mean input level during photostimulation for all laser intensities used in current-clamp experiments (right, 4-ms ISI). (**c**) Current-clamp recordings (CC) of CA1PC responses to CA3SC photostimulation before and after $GABA_A R$ blockade. (**d**) Input-output function for example CA1PC shown in **a**–**c**. Laser intensities used in example traces are marked with arrows. (**e**) Confocal image stacks of PSAM[L141F]-GlyR/tdTomato-expressing interneurons (tdTomato fluorescence pseudo-colored to black on a white background) in *Gad65-cre* mice and overlay (native red tdTomato color) with ChR2-sfGFP expression in the CA3SCs (green). (**f**) Two-photon image stack of recorded interneuron (IN, white), ChR2-sfGFP+ CA3SCs (green), and PSAM[L141F]-GlyR/tdTomato+ interneurons (red), and responses to somatic current injection and CA3SC photostimulation before and after bath application of 3 μM PSEM[308]. (**g**) Summary plots of firing rates recorded in PSAM[L141F]-GlyR+ interneurons in response to CA3SC photostimulation (input measured as CA1PC $\overline{I}_{Esyn}$) and somatic current injection (I_{inj}). (**h**) Current-clamp recordings from a CA1PC during CA3SC photostimulation in control conditions, after silencing GAD65+ interneurons with PSEM[308], and after subsequent application of gabazine. (**i**) Summary input-output function for CA1PCs comparing control conditions, pharmacogenetic removal of inhibition by silencing GAD65+ interneurons, and blockade of $GABA_A Rs$ (20 μM gabazine). Error bars indicate ± s.e.m.
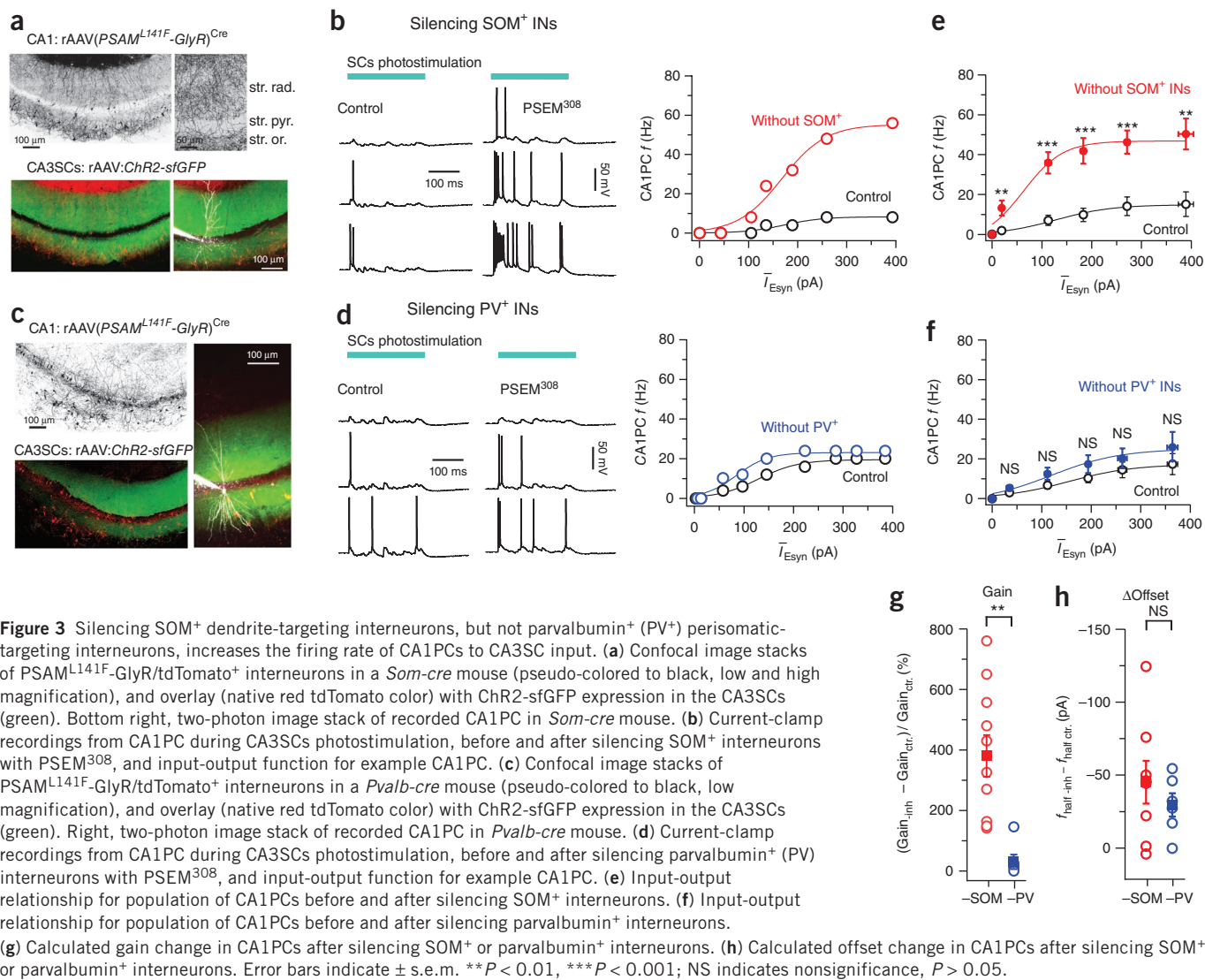
82 ± 12 pA; **Fig. 2i**). By confirming the selective silencing of genetically defined interneurons during CA3SC input, these data justify the use of this approach to investigate the influence of GABAergic interneuron subtypes on the CA1PC input-output transformation.

Dendrite-targeting interneurons regulate CA1PC firing rate

To silence a major subpopulation of dendrite-targeting interneurons in CA1, we generated knock-in mice expressing the Cre recombinase under the control of the somatostatin (*Som*, also known as *Sst*) promoter (*Som-cre*, see Online Methods). Consistent with previous findings[15,16,37,38], Cre-positive interneurons in *Som-cre* mice had axonal arborizations in strata oriens, radiatum and lacunosum-moleculare of the CA1 area, overlapping with the dendritic regions of CA1PCs and excluding the perisomatic regions (**Fig. 3a** and **Supplementary Fig. 3a–e,i,j**). Viral expression of PSAM[L141F]-GlyR in somatostatin-expressing interneurons was highly efficient (labeling efficiency = 84 ± 11%, *n* = 15; **Supplementary Fig. 3f**) and we observed complete and selective silencing following bath application of PSEM[308] (11 out of 11 SOM+ interneurons; **Supplementary Fig. 3g,h**). Silencing SOM+ interneurons during phasic CA3SC photostimulation caused a robust increase in the maximal firing rate of CA1PCs (from 15.2 ± 5 Hz to 50.4 ± 6 Hz, *n* = 12, *P* < 0.001), revealing a marked divisive influence of dendritic inhibition on the CA1PC

input-output transformation (Δgain/gain = 381 ± 57%, *n* = 12; Δoffset = 45 ± 15 pA, *n* = 12; **Fig. 3**). These results indicate that removal of dendritic inhibitory input is sufficient to increase the firing rate of CA1PCs in response to excitatory synaptic input.

To test whether dendritic inhibition is necessary to effectively regulate the CA1PC firing rate, we drove conditional expression of PSAM[L141F]-GlyR in parvalbumin-expressing interneurons of *Pvalb-cre* mice. These conditions permitted the silencing of predominantly perisomatic inhibition[19] while keeping dendritic inhibitory circuits intact (**Fig. 3c**, **Supplementary Fig. 4a–c** and Online Methods). Despite high expression of PSAM[L141F]-GlyR in parvalbumin+ interneurons (labeling efficiency = 84 ± 9%, *n* = 15; **Supplementary Fig. 4d**) and complete silencing following application of PSEM[308] (five of five interneurons; **Supplementary Fig. 4e,f**), this perturbation resulted in only a minor change in the CA1PC firing rate (maximum firing rate, from 17.2 ± 5 Hz to 26.2 ± 8 Hz, *P* = 0.244; Δgain/gain, 30 ± 23%; Δoffset, 29.6 ± 8 pA, *n* = 12; **Fig. 3d,f–h**). The inability of perisomatic inhibition to significantly regulate CA1PC firing rate could not be explained by ineffective activation of parvalbumin+ interneurons by the CA3SCs, as these cells fired at high frequencies even to low levels of photostimulation (**Supplementary Fig. 4g**). Furthermore, CA1PC firing rates did not further increase when parvalbumin+ interneuron silencing was complemented with bath application of the CB_1

Figure 3 Silencing SOM+ dendrite-targeting interneurons, but not parvalbumin+ (PV+) perisomatic-targeting interneurons, increases the firing rate of CA1PCs to CA3SC input. (**a**) Confocal image stacks of $PSAM^{L141F}$-GlyR/tdTomato+ interneurons in a *Som-cre* mouse (pseudo-colored to black, low and high magnification), and overlay (native red tdTomato color) with ChR2-sfGFP expression in the CA3SCs (green). Bottom right, two-photon image stack of recorded CA1PC in *Som-cre* mouse. (**b**) Current-clamp recordings from CA1PC during CA3SCs photostimulation, before and after silencing SOM+ interneurons with PSEM[308], and input-output function for example CA1PC. (**c**) Confocal image stacks of $PSAM^{L141F}$-GlyR/tdTomato+ interneurons in a *Pvalb-cre* mouse (pseudo-colored to black, low magnification), and overlay (native red tdTomato color) with ChR2-sfGFP expression in the CA3SCs (green). Right, two-photon image stack of recorded CA1PC in *Pvalb-cre* mouse. (**d**) Current-clamp recordings from CA1PC during CA3SCs photostimulation, before and after silencing parvalbumin+ (PV) interneurons with PSEM[308], and input-output function for example CA1PC. (**e**) Input-output relationship for population of CA1PCs before and after silencing SOM+ interneurons. (**f**) Input-output relationship for population of CA1PCs before and after silencing parvalbumin+ interneurons. (**g**) Calculated gain change in CA1PCs after silencing SOM+ or parvalbumin+ interneurons. (**h**) Calculated offset change in CA1PCs after silencing SOM+ or parvalbumin+ interneurons. Error bars indicate ± s.e.m. **$P < 0.01$, ***$P < 0.001$; NS indicates nonsignificance, $P > 0.05$.

receptor agonist WIN-55,212-2 (1 μM), which reduces GABAergic release from a separate population of perisomatic-targeting interneurons that express cholecystokinin[39] (**Supplementary Fig. 4h**). Together, these results indicate that dendritic inhibition, but not perisomatic inhibition, effectively regulates the gain of CA1PC input-output transformations.

Local inhibition of dendritic spikes and burst spiking

The increase in CA1PC firing rate following silencing of SOM+ dendrite-targeting interneurons was characterized by a switch to burst-spiking output mode in response to CA3SC input, reflected in a large increase in the duration of the initial slow depolarization underlying spikes measured at the soma (*Som-cre*, 508 ± 72% of control, $n = 12$; **Fig. 4a**). CA1PCs also switched to burst-spiking output mode following the complete removal of inhibition from CA1, but not following silencing of parvalbumin+ perisomatic-targeting interneurons (gabazine, 1,080 ± 121% of control, $n = 22$; *Gad65-cre*, 886 ± 171%, $n = 6$; *Pvalb-cre*, 120 ± 8%, $n = 11$; **Fig. 4a**). Given that dendritic nonlinearities contribute to somatic burst spiking[8,40,41], dendritic inhibition may regulate this switch to burst spiking by gating active dendritic electrogenesis. To test this possibility, we performed whole-cell recordings from distal parts of the main apical dendrites

of CA1PCs. Consistent with the proposed role for local inhibition in constraining dendritic spike generation[8,23,25], CA3SC photostimulation evoked large-amplitude dendritic spikes when dendrite targeting interneurons were silenced, but not when only perisomatic targeting interneurons were silenced (*Gad65-cre*, $n = 2$; *Som-cre*, $n = 3$; *Pvalb-cre*, $n = 3$; **Fig. 4b**). These results indicate that a reduction in dendritic inhibition is required to allow dendritic electrogenesis, which switches the output mode of CA1PCs to burst spiking.

Thin basal and apical oblique dendrites of CA1PCs, which receive the majority of glutamatergic input from the CA3SCs, primarily generate local Na+/NMDAR-dependent spikes[10,28], whereas the distal apical trunk and dendritic tuft support global Ca^{2+} and NMDA plateau spikes[25,41,42]. Because SOM+ neurons primarily inhibit thin dendrites[14–16,22], we reasoned that pharmacological blockade of NMDARs would reduce the local dendritic electrogenesis and burst spiking that we observed after silencing SOM+ interneurons. Indeed, bath application of the NMDAR antagonist D,L-2-amino-5-phosphonovaleric acid (D,L-AP5, 100 μM) abolished dendritic electrogenesis ($n = 1$; **Fig. 4c**), somatic burst spiking and firing rate increases induced by silencing SOM+ interneurons (maximum firing rate, from 52.2 ± 8 Hz to 17.2 ± 3 Hz, $P < 0.05$, $n = 3$; somatic burst duration, from 648 ± 72% to 88 ± 9% of control, $P < 0.05$, $n = 3$; **Fig. 4d**). In contrast, when inhibition

Figure 4 Dendrite-targeting interneurons inhibit NMDAR-dependent dendritic nonlinearities and burst spiking. (**a**) Summary plot of calculated change in somatic burst duration from control conditions during CA3SC photostimulation following pharmacological blockade of inhibition (20 μM gabazine, black) and pharmacogenetic silencing of GAD65$^+$ (gray), SOM$^+$ (red) or parvalbumin$^+$ (blue) interneurons. (**b**) Schematic and two-photon image stacks of patch-clamp recordings from the distal apical dendrites of CA1PCs (left; CA1PCs, white; ChR2-sfGFP$^+$ CA3SCs, green; PSAM^{L141F}-GlyR/tdTomato$^+$ interneurons, red) in *Gad65-cre*, *Som-cre* and *Pvalb-cre* mice. Current-clamp recordings from the distal apical dendrites in control conditions and following pharmacogenetic silencing of GAD65$^+$, SOM$^+$ or parvalbumin$^+$ interneurons during CA3SC photostimulation (right). Note the prominent local spikes recorded from the dendrites of CA1PCs following silencing of GAD65$^+$ and SOM$^+$ interneurons, but not following silencing of parvalbumin$^+$ interneurons. Further pharmacological blockade of inhibition (20 μM gabazine) was required to induce dendritic spikes in these cells (bottom trace). (**c**) Intracellular recording from CA1PC apical dendrite during CA3SCs photostimulation in *Som-cre* mice, showing the effect of NMDAR blockade (100 μM D,L-AP5) on dendritic spiking induced by SOM$^+$ interneuron silencing. (**d**) Summary plots of maximum firing rate and burst duration measured in CA1PCs to CA3SC photostimulation during pharmacological blockade of inhibition (20 μM gabazine, black) or pharmacogenetic silencing of SOM$^+$ interneurons (red), and after subsequent blockade of NMDARs with D,L-AP5 (gray). Error bars indicate ± s.e.m. *$P < 0.05$, **$P < 0.01$, ***$P < 0.001$.
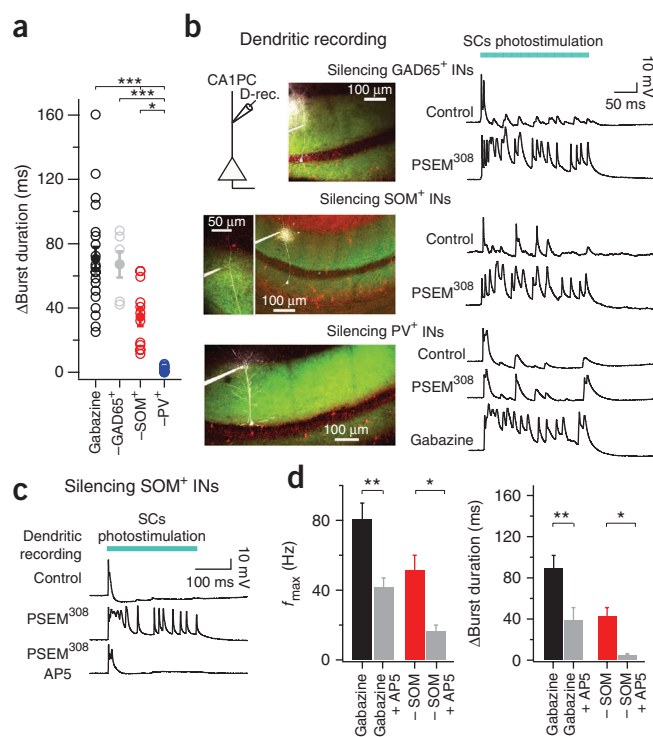
was completely removed from the entire somatodendritic axis of CA1PCs (20 μM gabazine), blockade of NMDARs only partially suppressed burst spiking (maximum firing rate, from 81.3 ± 9 Hz to 42.1 ± 5 Hz, $P < 0.01$; somatic burst duration, from 1,130 ± 120% to 580 ± 110%, $P < 0.01$, $n = 6$; **Fig. 4d**). These data indicate that SOM$^+$ dendrite-targeting interneurons primarily influence the transformation of CA3SC input into spike output by inhibiting NMDAR-dependent branch-specific nonlinearities in CA1PC radial oblique and basal dendrites. A more pronounced suppression of inhibition allows for more global spiking, perhaps including Ca^{2+} electrogenesis in the apical trunk and tuft[41].

Cell type–specific disinhibition in CA1

The minimal influence of perisomatic-targeting interneurons on the suprathreshold input-output transformation was surprising to us given the detectable effect of perisomatic inhibitory conductance on the single-branch subthreshold input-output relationship (**Fig. 1**). We hypothesized that this may reflect synaptic interactions between perisomatic and dendritic inhibitory circuits, which are not engaged in uncaging experiments. We first tested this hypothesis by examining the connectivity between inhibitory interneurons using ChR2-mediated photostimulation. In slices from *Pvalb-cre* mice injected with rAAV(*ChR2-sfGFP*)^{Cre} into dorsal CA1, we photostimulated parvalbumin$^+$ perisomatic-targeting interneurons and recorded ChR2-evoked inhibitory postsynaptic responses in parvalbumin$^-$ interneurons in strata pyramidale and oriens/alveus of CA1 (parvalbumin$^-$, $n = 18$, **Fig. 5a**). Bistratified interneurons, identified by *post hoc* somatostatin immunoreactivity and axonal arborization confined to strata oriens and radiatum[14,21,43], received large-amplitude GABAergic input from parvalbumin$^+$ interneurons[44]. In contrast, oriens-lacunosum-moleculare (O-LM) cells[43], with somata located in stratum oriens and axons targeting the distal dendritic tuft of CA1PCs, received small-amplitude inputs (SOM$^+$ bistratified, 9.07 ± 2.8 nS, $n = 3$; O-LM, 0.94 ± 0.4 nS, $n = 7$; **Fig. 5a,b** and **Supplementary Fig. 5a**). To test the relevance of this connectivity to CA1 circuit processing, we measured the input-output transformation of dendrite-targeting interneurons during CA3SC photostimulation,

before and after silencing parvalbumin$^+$ perisomatic interneurons. Indeed, the firing rates of proximal dendrite-targeting interneurons markedly increased ($n = 3$; **Fig. 5c,d**), whereas the firing rates of interneurons targeting the distal dendritic tuft of CA1PCs were unchanged ($n = 5$; **Supplementary Fig. 5b–d**). Furthermore, we found that distal inhibition of the dendritic tuft minimally affected responses to CA3SC input (**Supplementary Fig. 6a–f**), but did regulate global dendritic Ca^{2+} spikes in distal dendrites (**Supplementary Fig. 6g–i**)[8,23,25]. This suggests that integration of CA3SC input in thin basal and oblique dendrites of CA1PCs is specifically regulated by co-aligned inhibition from bistratified cells, which are strongly inhibited by parvalbumin$^+$ perisomatic-targeting interneurons. This disinhibitory network interaction resulted in a compartmentalized switch in GABAergic conductance, as silencing parvalbumin$^+$ perisomatic-targeting interneurons decreased somatic and increased dendritic inhibitory conductance during CA3SC input (**Fig. 5e,f**).

Finally, we found that silencing of SOM$^+$ dendrite-targeting interneurons increased the firing rate of fast-spiking basket cells ($n = 5$) and decreased somatic input resistance in CA1PCs (**Supplementary Fig. 7**). This finding is most likely the result of a combination of removing direct inhibition from SOM$^+$ interneurons (4.58 ± 0.6 nS, $n = 3$; **Supplementary Fig. 7a**) and increasing feedback excitation from CA1PCs. However, this disinhibition of basket cells was not able to compensate for CA1PC burst firing following the removal of dendritic inhibition. These circuit behaviors were captured in a conductance-based multicompartmental model[45] (**Fig. 5g** and Online Methods) showing that the asymmetry of dendritic and perisomatic inhibitory control over CA1PC input processing was augmented by synaptic disinhibition between these GABAergic populations. For strengths of interneuron-interneuron connectivity similar to those observed experimentally, a disinhibitory increase in dendritic inhibition fully compensated for the removal of perisomatic inhibition on CA1PC firing rates, whereas disinhibitory increases in perisomatic inhibition only moderately suppressed the effect of silencing dendritic inhibition (**Fig. 5g**).
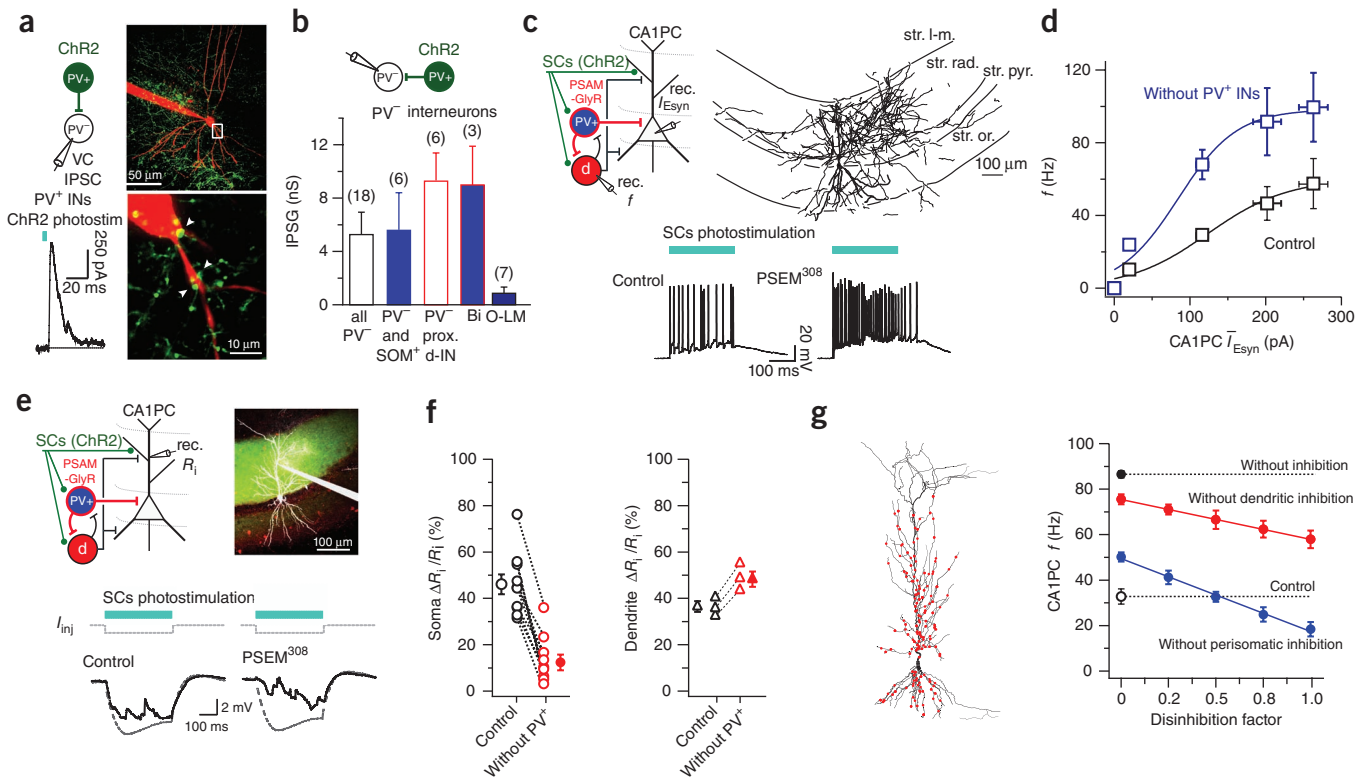
Figure 5 Cell type–specific disinhibition within the local inhibitory network. (**a**) Schematic of recording configuration and example IPSG in parvalbumin⁻ interneuron to photostimulating parvalbumin⁺ interneurons expressing ChR2 (left, voltage clamp at −40 mV). Right, two-photon stack of a parvalbumin⁻ interneuron (red) in str. oriens of CA1 in a slice expressing ChR2-sfGFP in parvalbumin⁺ interneurons (green). The boxed region shows putative contacts (white arrowheads). (**b**) Mean ChR2 photostimulation–evoked IPSG from parvalbumin⁻ cells in *Pvalb-cre* mice, subdivided as all parvalbumin⁻ interneurons, SOM⁺ cells (six of ten parvalbumin⁻ interneurons tested for somatostatin immunoreactivity), all proximal dendrite-targeting interneurons (prox. d-IN, axons in strata oriens/radiatum), bistratified cells (Bi) and O-LM cells. (**c**) Schematic and morphological reconstruction of a proximal dendrite-targeting parvalbumin⁻ interneuron (top, thin lines are axons). Current-clamp recordings from the reconstructed interneuron during CA3SCs photostimulation in control and after silencing parvalbumin⁺ interneurons. (**d**) Summary of input-output relationship for proximal dendrite-targeting interneurons before and after parvalbumin⁺ silencing. (**e**) Schematic and two-photon stack of dendritic recording from CA1PC from *Pvalb-cre* mouse (top; CA1PCs, white; ChR2-sfGFP⁺ CA3SCs, green; PSAM^L141F-GlyR/tdTomato⁺ interneurons, red). Example dendritic voltage traces of CA1PC input resistance during CA3SC input in control and after silencing parvalbumin⁺ interneurons are shown. (**f**) Summary of changes to somatic and dendritic input resistance in control and after silencing parvalbumin⁺ interneurons, reflecting changes in inhibitory synaptic conductance. (**g**) Geometry of multicompartmental CA1PC model (excitatory synapse locations in red) and plot of CA1PC firing rate for various levels of disinhibition when either perisomatic or dendritic inhibition is silenced (control and no inhibition conditions are shown for comparison, excitation remains constant). Error bars indicate ± s.e.m.

Our results indicate that parvalbumin⁺ interneurons inhibit interneurons targeting the proximal dendrites of CA1PCs during CA3SC input, the release of which can compensate for a withdrawal of perisomatic inhibition and amplify the asymmetry of perisomatic and dendritic inhibition on CA1PC firing rates. This important synaptic interaction between inhibitory circuit elements shapes excitatory synaptic integration by switching inhibitory conductance from one compartment of CA1PCs to another.

DISCUSSION

Selectively silencing genetically defined local inhibitory interneurons allowed us to identify dendritic inhibition as an important regulator of burst spiking in CA1 pyramidal neurons. Dendritic inhibition was more effective than perisomatic inhibition at regulating excitatory synaptic integration, a difference that was amplified in active networks through interactions in the local inhibitory circuitry. From a computational perspective, our results suggest that the role of dendritic inhibition is primarily to regulate the gain of pyramidal neuron input-output transformations, which greatly expands the dynamic range over which cells can produce rate changes in the presence of

active dendritic electrogenesis. We also found that the influence of dendritic inhibition on pyramidal cells can be tuned by the activity of perisomatic-targeting interneurons through asymmetric disinhibition. This organization may permit flexible and state-dependent extrinsic modulation over pyramidal cell output through interneuron-specific targeting with long-range subcortical inputs[46,47].

We found that silencing of somatostatin-expressing interneurons accounts for about half of the firing rate and burst duration change observed during complete removal of inhibition. This demonstrates the importance of somatostatin-expressing bistratified interneurons in CA1PC processing of CA3SC input, but suggests that other interneuron classes targeting dendrites in strata oriens and radiatum also contribute to regulating dendritic integration and electrogenesis in CA1PCs. Indeed, the differential firing of bistratified[22], Schaffer collateral–associated[48], apical dendrite innervating and Ivy cells[49] during networks oscillations *in vivo* suggest that these interneurons may regulate CA3SC input integration in a state-dependent manner. Other classes of dendrite-targeting interneurons that inhibit the distal tuft, such as O-LM, perforant path–associated or neurogliaform cells[16,21], may contribute to regulating the interaction between CA3SC

input and input to the distal dendritic tuft from the entorhinal cortex during generation of global NMDAR and Ca^{2+} plateau spikes[41,45].

Our findings support a multimodal synaptic integration scheme in hippocampal CA1PCs (**Supplementary Fig. 8**), in which the initiation of local NMDAR-dependent spikes in radial oblique and basal dendrites, the predominant regenerative event in these thin branches[10], is primarily regulated by co-aligned inhibition. A suppression of dendritic inhibition of thin dendrites allows for the generation of local NMDAR spikes and somatic burst spiking, whereas a more complete removal of dendritic inhibition allows the output of thin dendrites to also recruit the Ca^{2+} spike initiation zone, presumably located in distal apical trunk or in the tuft region, and to generate global Ca^{2+} and NMDAR plateau spiking[25,41]. Thus, our results suggest that the compartmentalized excitatory synaptic integration scheme proposed recently for neocortical layer 5 pyramidal neurons[24] may also apply to excitatory integration in hippocampal CA1 pyramidal neurons. Our results further suggest that subcellular domain-specific inhibitory circuits are involved in this compartmentalized integration scheme.

From a behavioral perspective, the relative amount of dendritic inhibition may determine the spiking behavior of CA1PCs in a particular environment during spatial navigation. Most CA1PCs could display the phenotype of a silent cell even under conditions of high excitation when accompanied by balanced levels of dendritic inhibition. A suppression of this inhibition could permit active dendritic integration in a subset of cells, resulting in sparse population coding in a given environment[11,12]. Context-dependent modulation of dendritic inhibitory circuits could also allow relative changes in the firing rates of place cells to encode nonspatial variables via rate remapping[6]. A diversity of dendrite-targeting interneurons could potentially serve to control different aspects of rate remapping in CA1, in which place fields and firing rates change to accommodate a variety of new contextual information introduced into the environment.

Our results, indicating that dendrite-targeting interneurons are involved in controlling CA1PC firing rate, complement previous studies documenting the role of perisomatic-targeting interneurons in the control of spike timing and network oscillations[17–19]. The distinctions between these inhibitory cell types adds functional implications to the wealth of anatomical and physiological data demonstrating the diversity of local GABAergic interneurons in the hippocampus[15,16]. Our data lend further evidence for a division of labor in cortical circuits, in which the tremendous heterogeneity of inhibitory interneurons has evolved to support diverse local circuit computations[13].

METHODS

Methods and any associated references are available in the online version of the paper at http://www.nature.com/natureneuroscience/.

Note: Supplementary information is available on the Nature Neuroscience website.

AUTHOR CONTRIBUTIONS
M.L.-B. and A.L. designed the study. M.L.-B., G.F.T. and A.L. performed all electrophysiological and anatomical experiments and analyzed the data. P.K. performed compartmental modeling. P.H.L. and S.M.S. provided constructs and compounds for the PSAM-PSEM method. F.B., X.-H.S. and J.F.N. synthesized and provided PENB-L-glutamate. B.V.Z. prepared plasmids, designed rAAV viruses and generated knock-in mouse lines. M.L.-B. and A.L. wrote the paper with the help of the other authors.

1. Kandel, E.R. & Spencer, W.A. Electrophysiology of hippocampal neurons II: after-potentials and repetitive firing. *J. Neurophysiol.* **24**, 243–259 (1961).
2. Thompson, L.T. & Best, P.J. Place cells and silent cells in the hippocampus of freely behaving rats. *J. Neurosci.* **9**, 2382–2390 (1989).
3. O'Keefe, J. & Dostrovsky, J. The hippocampus as a spatial map. Preliminary evidence from unit activity in the freely-moving rat. *Brain Res.* **34**, 171–175 (1971).
4. O'Keefe, J. & Nadel, L. *The Hippocampus as a Cognitive Map* (Oxford University Press, Oxford, 1978).
5. Ahmed, O.J. & Mehta, M.R. The hippocampal rate code: anatomy, physiology, and theory. *Trends Neurosci.* **32**, 329–338 (2009).
6. Colgin, L.L., Moser, E.I. & Moser, M.-B. Understanding memory through hippocampal remapping. *Trends Neurosci.* **31**, 469–477 (2008).
7. Nevian, T., Larkum, M.E., Polsky, A. & Schiller, J. Properties of basal dendrites of layer 5 pyramidal neurons: a direct patch-clamp recording study. *Nat. Neurosci.* **10**, 206–214 (2007).
8. Larkum, M.E., Zhu, J.J. & Sakmann, B. A new cellular mechanism for coupling inputs arriving at different cortical layers. *Nature* **398**, 338–341 (1999).
9. Gasparini, S. & Magee, J.C. State-dependent dendritic computation in hippocampal CA1 pyramidal neurons. *J. Neurosci.* **26**, 2088–2100 (2006).
10. Losonczy, A. & Magee, J.C. Integrative properties of radial oblique dendrites in hippocampal CA1 pyramidal neurons. *Neuron* **50**, 291–307 (2006).
11. Harvey, C.D., Collman, F., Dombeck, D.A. & Tank, D.W. Intracellular dynamics of hippocampal place cells during virtual navigation. *Nature* **461**, 941–946 (2009).
12. Epsztein, J., Brecht, M. & Lee, A.K. Intracellular determinants of hippocampal CA1 place and silence cell activity in a novel environment. *Neuron* **70**, 109–120 (2011).
13. Isaacson, J.S. & Scanziani, M. How inhibition shapes cortical activity. *Neuron* **72**, 231–243 (2011).
14. Buhl, E.H., Halasy, K. & Somogyi, P. Diverse sources of hippocampal unitary inhibitory postsynaptic potentials and the number of synaptic release sites. *Nature* **368**, 823–828 (1994).
15. Freund, T.F. & Buzsáki, G. Interneurons of the hippocampus. *Hippocampus* **6**, 347–470 (1996).
16. Klausberger, T. & Somogyi, P. Neuronal diversity and temporal dynamics: the unity of hippocampal circuit operations. *Science* **321**, 53–57 (2008).
17. Cobb, S.R., Buhl, E.H., Halasy, K., Paulsen, O. & Somogyi, P. Synchronization of neuronal activity in hippocampus by individual GABAergic neurons. *Nature* **378**, 75–78 (1995).
18. Pouille, F. & Scanziani, M. Enforcement of temporal fidelity in pyramidal cells by somatic feed-forward inhibition. *Science* **293**, 1159–1163 (2001).
19. Losonczy, A., Zemelman, B.V., Vaziri, A. & Magee, J.C. Network mechanisms of theta related neuronal activity in hippocampal CA1 pyramidal neurons. *Nat. Neurosci.* **13**, 967–972 (2010).
20. Megías, M., Emri, Z., Freund, T.F. & Gulyas, A.I. Total number and distribution of inhibitory and excitatory synapses on hippocampal CA1 pyramidal cells. *Neuroscience* **102**, 527–540 (2001).
21. Klausberger, T. GABAergic interneurons targeting dendrites of pyramidal cells in the CA1 area of the hippocampus. *Eur. J. Neurosci.* **30**, 947–957 (2009).
22. Klausberger, T. *et al.* Spike timing of dendrite-targeting bistratified cells during hippocampal network oscillations *in vivo. Nat. Neurosci.* **7**, 41–47 (2004).
23. Murayama, M. *et al.* Dendritic encoding of sensory stimuli controlled by deep cortical interneurons. *Nature* **457**, 1137–1141 (2009).
24. Larkum, M.E., Nevian, T., Sandler, M., Polsky, A. & Schiller, J. Synaptic integration in tuft dendrites of layer 5 pyramidal neurons: a new unifying principle. *Science* **325**, 756–760 (2009).
25. Miles, R., Tóth, K., Gulyás, A.I., Hájos, N. & Freund, T.F. Differences between somatic and dendritic inhibition in the hippocampus. *Neuron* **16**, 815–823 (1996).
26. Collingridge, G.L., Herron, C.E. & Lester, R.A.J. Synaptic activation of *N*-methyl-D-aspartate receptors in the Schaffer collateral–commissural pathway of rat hippocampus. *J. Physiol. (Lond.)* **399**, 282–300 (1988).
27. Poirazi, P., Brannon, T. & Mel, B.W. Pyramidal neuron as 2-layer neural network. *Neuron* **37**, 989–999 (2003).
28. Losonczy, A., Makara, J.K. & Magee, J.C. Compartmentalized dendritic plasticity and input feature storage in neurons. *Nature* **452**, 436–441 (2008).
29. Branco, T. & Häusser, M. The single dendritic branch as a fundamental functional unit in the nervous system. *Curr. Opin. Neurobiol.* **20**, 494–502 (2010).
30. Rial Verde, E.M., Zayat, L., Etchenique, R. & Yuste, R. Photorelease of GABA with visible light using an inorganic caging group. *Front. Neural Circuits* **2**, 2 (2008).
31. Williams, S.R. Spatial compartmentalization and functional impact of conductance in pyramidal neurons. *Nat. Neurosci.* **7**, 961–967 (2004).

32. Williams, S.R. & Stuart, G.J. Dependence of EPSP efficacy on synapse location in neocortical pyramidal neurons. *Science* **295**, 1907–1910 (2002).

33. Knowles, W.D. & Schwartzkroin, P.S. Axonal ramifications of hippocampal CA1 pyramidal cells. *J. Neurosci.* **1**, 1236–1241 (1981).

34. Buzsáki, G. Theta oscillations in the hippocampus. *Neuron* **33**, 325–340 2002).

35. Magnus, C.J. *et al.* Chemical and genetic engineering of selective ligand-ion channel interactions. *Science* **333**, 1292–1296 (2011).

36. Atasoy, D., Aponte, Y., Su, H.H. & Sternson, S.M.A. FLEX switch targets Channelrhodopsin-2 to multiple cell types for imaging and long-range circuit mapping. *J. Neurosci.* **28**, 7025–7030 (2008).

37. Losonczy, A., Zhang, L., Shigemoto, R., Somogyi, P. & Nusser, Z. Cell type dependence and variability in the short-term plasticity of EPSCs in identified mouse hippocampal interneurons. *J. Physiol. (Lond.)* **542**, 193–210 (2002).

38. Klausberger, T. *et al.* Brain state– and cell type–specific firing of hippocampal interneurons *in vivo. Nature* **421**, 844–848 (2003).

39. Katona, I. *et al.* Presynaptically located CB1 cannabinoid receptors regulate GABA release from axon terminals of specific hippocampal interneurons. *J. Neurosci.* **19**, 4544–4558 (1999).

40. Magee, J.C. & Carruth, M. Dendritic voltage-gated ion channels regulate the action potential firing mode of hippocampal CA1 pyramidal neurons. *J. Neurophysiol.* **82**, 1895–1901 (1999).

41. Takahashi, H. & Magee, J.C. Pathway interactions and synaptic plasticity in the dendritic tuft regions of CA1 pyramidal neurons. *Neuron* **62**, 102–111 (2009).

42. Golding, N.L., Jung, H.Y., Mickus, T. & Spruston, N. Dendritic calcium spike initiation and repolarization are controlled by distinct potassium channel subtypes in CA1 pyramidal neurons. *J. Neurosci.* **19**, 8789–8798 (1999).

43. Maccaferri, G., Roberts, J.D., Szucs, P., Cottingham, C.A. & Somogyi, P. Cell surface domain specific postsynaptic currents evoked by identified GABAergic neurones in rat hippocampus *in vitro. J. Physiol. (Lond.)* **524**, 91–116 (2000).

44. Cobb, S.R. *et al.* Synaptic effects of identified interneurons innervating both interneurons and pyramidal cells in the rat hippocampus. *Neuroscience* **79**, 629–648 (1997).

45. Jarsky, T., Roxin, A., Kath, W.L. & Spruston, N. Conditional dendritic spike propagation following distal synaptic activation of hippocampal CA1 pyramidal neurons. *Nat. Neurosci.* **8**, 1667–1676 (2005).

46. Mulligan, K.A. & Törk, I. Serotoninergic innervation of the cat cerebral cortex. *J. Comp. Neurol.* **270**, 86–110 (1988).

47. Varga, V. *et al.* Fast synaptic subcortical control of hippocampal circuits. *Science* **326**, 449–453 (2009).

48. Cope, D.W. *et al.* Cholecystokinin-immunopositive basket and Schaffer collateral– associated interneurons target different domains of pyramidal cells in the CA1 area of the rat hippocampus. *Neuroscience* **109**, 63–80 (2002).

49. Fuentealba, P. *et al.* Ivy cells: a population of nitric oxide–producing, slow-spiking GABAergic neurons and their involvement in hippocampal network activity. *Neuron* **57**, 917–929 (2008).

ONLINE METHODS

All experiments were conducted in accordance with the US National Institutes of Health guidelines and with the approval of the Columbia University Institutional Animal Care and Use Committee.

Preparation of knock-in mice and viruses. *Gad65-cre*, *Pvalb-cre* and *Som-cre* knock-in mice were generated using homologous targeting constructs to insert an internal ribosome entry site (*IRES*) followed by the Cre recombinase coding sequence into the 3′ UTR of the respective mouse genes. Constructs were electroporated into hybrid C57BL/6-129/SV stem cells, with colonies screened using PCR analysis for correct construct integration. Progeny carrying the transgene were bred to homozygosity. *Som-cre* and *Pvalb-cre* mice were maintained as a mixed strain. *Gad65-cre* mice were backcrossed repeatedly to C57BL/6 and maintained as a C57BL/6 strain. The *loxP-STOP-loxP-tdTomato* Cre reporter strain B6;129S6-*Gt(ROSA)26Sor^{tm9(CAG-tdTomato)Hze}*/J (Jackson Laboratory) was bred with *Gad65-cre* mice to express tdTomato in the GABAergic cells of the double-hemizygous *Gad65-cre; tdTomato* progeny. For electrophysiology experiments, both homozygous and hemizygous (bred with C57BL/6) Cre-expressing mice were used. No differences in the intrinsic properties of CA1PCs or in the effect of PSAM^{L141F}-GlyR between homozygous and hemizygous mice were found, therefore the data were pooled. For anatomical characterization, homozygous or hemizygous *Gad65-cre* and hemizygous *Som-cre* and *Pvalb-cre* mice were used.

PSAM^{L141F}-GlyR was constructed from a mutated (L141F) alpha 7 nAChR ligand binding domain fused to the ion pore domain of the glycine receptor and was codon-optimized for the mouse. PSEM^{308} is a second-generation ligand for PSAM^{L141F}-GlyR that shows improved potency properties. The details of PSEM^{308} and its properties are described elsewhere.

To prepare Cre-independent rAAV:*ChR2-sfGFP*, we joined the codon-optimized coding sequence of *ChR2* (1-304, H134R) to that of superfolder GFP (sfGFP) using the 10 amino acid linker EAGAVSGGVV, and cloned into a recombinant adeno-associated virus (rAAV) cassette containing the human *synapsin* promoter (*SYN*), a woodchuck post-transcriptional regulatory element (*WPRE*), SV40 polyadenylation sequence and two inverted terminal repeats. To prepare Cre-dependent rAAV(*ChR2-sfGFP*)^{Cre}, rAAV(*sfGFP*)^{Cre}, rAAV(*tdTomato*)^{Cre} and rAAV(*PSAM^{L141F}-GlyR*)^{Cre}, we cloned the respective coding sequences into the same vector in the inverted (with respect to promoter) orientation. Viruses were assembled using a modified helper-free system (Stratagene) as a serotypes 2/1 (*rep/cap* genes) for rAAV:*ChR2-sfGFP* and as serotype 2/7 for the Cre-dependent constructs.

Viral injection. Viruses were stereotaxically injected into the dorsal hippocampi of adult mice using thin glass pipettes (10-μm tip diameter) and Nanoject II injectors (Drummond Scientific). Virus was injected into bilateral dorsal CA3 (rAAV:*ChR2-sfGFP*; 6 penetrations, 2 injections per penetration) and dorsal CA1 (rAAV(*PSAM^{L141F}-GlyR*)^{Cre} and rAAV(*tdTomato*)^{Cre}, 3:1 ratio, 4 penetrations, 5–7 injections per penetration). In separate experiments, rAAV(*ChR2-sfGFP*)^{Cre} was injected into dorsal CA1 (three penetrations, five injections per penetration). Individual injections of ~30 nl high-titer virus were made in each pipette penetration along the *z* axis of the tract as pipettes were withdrawn dorsally. Mice were returned to their home cage for 4–6 weeks before acute slice preparation.

Slice preparation and electrophysiology. Coronal slices (350 μm) were prepared from the dorsal hippocampus of adult mice, as described previously[10]. Slices were secured on mesh in a custom-made double-perfusion recording chamber, and perfused over both sides at 5–7 ml min^{-1} with artificial cerebrospinal fluid (ACSF) maintained at 32–33 °C and containing 125 mM NaCl, 25 mM NaHCO$_3$, 2.5 mM KCl, 1.25 mM NaH$_2$PO$_4$, 1 mM MgCl$_2$, 2 mM CaCl$_2$, 22.5 mM glucose, 3 mM sodium pyruvate and 1 mM ascorbate, and saturated with 95% O$_2$ and 5% CO$_2$. During most recordings, 500 nM CGP55845 (Tocris) was added to the ACSF. Slices were visualized with Dodt contrast optics using a Zeiss Examiner. Z1 with a 40× objective (NA = 0.75) for somatic recordings and 63× objective (NA = 1.0) for dendritic recordings (Zeiss). Neurons expressing sfGFP or tdTomato, or containing Alexa 594/488, were imaged with a two-photon scanning upright microscope (Prairie Technologies).

Whole-cell patch-clamp recordings from somata or dendrites of CA1 pyramidal neurons or from somata of CA1 interneurons were obtained using a Dagan BVC-700A amplifier in the active 'bridge' mode, filtered at 1–10 kHz and digitized at 50 kHz. Recording pipettes were pulled from borosilicate glass to tip resistances of ~4–7 MΩ for somatic recordings and ~8–10 MΩ for dendritic recordings and contained 130 mM potassium gluconate, 8 mM KCl, 4 mM NaCl, 10 mM HEPES, 4 mM Mg$_2$ATP, 0.3 mM Tris$_2$GTP, 14 mM phosphocreatine, and 0.1 mM Alexa 594 or Alexa 488, pH 7.25. Biocytin (0.2%, wt/vol, Sigma) was included in the intracellular solution for recordings from interneurons. In current-clamp recordings, membrane potential was kept close to the GABA$_A$R reversal measured in voltage clamp (~−65 mV).

PENB-L-caged glutamate was prepared from 2-(5-iodo-2-nitrophenyl)propan-1-ol and 4-*tris*-ethoxy(methoxy) phenylboronic acid (**Supplementary Fig. 9**). The details of synthesis of PENB-L-caged glutamate and its properties are described elsewhere. Two-photon glutamate uncaging was performed as described previously[10]. Briefly, the presentation of variable spatio-temporal input patterns was performed using a dual galvanometer–based scanning system (Prairie Technologies) to photo-release glutamate at multiple dendritic spines. Ultra-fast, pulsed laser light (Chameleon Ultra II, Coherent) at 920–930 nm was used to excite Alexa 594 or Alexa 488, whereas 740 nm was used to photolyze PENB-L-caged glutamate (2 mM applied via broken pipette above slice). Because of the high two-photon cross-section of PENB-L-caged glutamate (Goppert-Mayer = 3.3 at 740 nm), we were able to use this compound in low concentration and without having a substantial antagonistic effect on GABA$_A$ receptors. For single-photon GABA uncaging, 80 or 160 μM Rubi-GABA was added to the puffer solution and a blue laser (473 nm, CrystaLaser) was coupled to the uncaging path of the scan-head. Experiments were conducted by first uncaging glutamate onto multiple (up to 40) spines of well-isolated dendrites (<60 μm below surface of the slice) asynchronously (with a 100-ms ISI) to evoke temporally isolated responses, and then to calculate the arithmetic sum of the individual two-photon EPSPs recorded at the soma (expected peak depolarization in **Fig. 1b,c** and **Supplementary Fig. 6c**). This expected linear sum was compared with the actually measured membrane potential response following glutamate uncaging onto the same sequence of spines in the presence and absence of Rubi-GABA uncaging placed near (<5 μm) the excited branch, near the soma (**Fig. 1**) or in the apical tuft (**Supplementary Fig. 6c**). During combined uncaging, one-photon GABA uncaging was followed by two-photon glutamate uncaging (1–5 ms ISI).

Photostimulation of CA3SCs. For ChR2 photostimulation of the CA3SCs, a blue DPSS laser (473 nm, CrystaLaser) was coupled to the uncaging path of the two-photon scan-head with a 20× objective to access the extent of ChR2-sfGFP$^+$ CA3SC axons in strata radiatum and oriens of CA1. Photostimuli consisted of 1-ms pulses in the range of 10–200 μW directed at the specimen. Timing, position and intensity of the laser pulses were controlled using the laser's analog modulation circuitry (PrairieView-TriggerSync, Prairie Technologies). A 6 × 8–point grid of stimulation points was spread over the CA1 strata radiatum/oriens, away from the recorded cell and toward CA3 to avoid direct ChR2-depolarization of terminals. Each point in the photostimulation grid (1–48) was stimulated once, sequentially in a random spatial order, with an ISI of 4 ms for phasic photostimulation or 74 ms for recording individual EPSCs. After recordings under various conditions in current-clamp mode (4-ms ISI), 20 μM SR95531 was added to the extracellular solution to block GABA$_A$ receptors, CA1PCs were voltage camped and grid photostimulation was repeated with 74-ms ISI. This allows EPSCs from each photostimulation point to be independently measured and summed together to estimate a 'mean input current' for laser intensities used in current-clamp experiments. This was repeated for all laser powers used throughout the experiment, and constituted the *x* axis of suprathreshold input-output curves. After recording the firing rate of interneurons, the pipette was removed and a pyramidal cell was patched in the vicinity of the interneuron (<50 μm) for mean currents to be measured with the same temporal order and spatial position of the grid as was used for the previously recorded interneuron. This gave a standard measure of synaptic input to compare the spike output from pyramidal cells and interneurons of different types across slices.

Under various conditions, CA1PC firing rates saturated at high levels of input, possibly reflecting biophysical constraints. However the possibility cannot be excluded that, at high photostimulation levels, partial overlap of laser foci for individual points in the grid could desensitize ChR2 in CA3SCs axons that are stimulated more than once. Any resulting reductions in input current during 4-ms ISI grid photostimulation would not have been fully detected when isolated EPSCs were measured given the relative temporal isolation (74-ms ISI).

This spatially dispersed and temporally asynchronous activation of the CA3SCs *in vitro* was designed to simulate the activity of CA3 ensembles during exploratory theta states *in vivo*, in which individual CA3PCs fire at low frequency and excite neurons in CA1 through high convergence[5,34]. The mean rate of presynaptic CA3SCs inputs during ChR2 photostimulation was estimated to range from ~0.2 up to 20 kHz, by averaging measured currents elicited from stimulating each individual photostimulation point in the 6×8 grid in isolation, dividing this single-point average by the CA3SCs unitary input measured at the soma (~10 pA)[5], and multiplying by the number of stimulation points over the stimulation time.

Drug application. PSEM[308] was dissolved in DMSO, stored in 100 mM aliquots, diluted in ACSF to a final concentration of 3 µM, and applied for 20–30 min for maximal effect. There was complete silencing of neurons expressing PSAM[L141F]-GlyR without changing the excitability of interneurons not expressing PSAM[L141F]-GlyR, or altering the intrinsic or input-output properties of pyramidal cells following bath application of PSEM[308] at this concentration (**Supplementary Figs. 2–4**). Other drugs used in our experiments include gabazine (20 µM, Tocris), D,L-AP5 (100 µM, Tocris), CGP55845A (500 nM, Tocris), 4-aminopyridine (2 mM, Sigma) and WIN-55,212-2 (1 µM, Tocris), which were dissolved in water or DMSO and diluted to final concentration in ACSF ([DMSO] < 0.005%).

Characterization of knock-in Cre mice. Adult heterozygous mice were deeply anesthetized with isoflurane and perfused first with 0.1 M phosphate-buffered saline (PBS, pH 7.4) and then with 4% paraformaldehyde (wt/vol). For light microscopic immunocytochemistry, sections (50 µm) were rinsed in PBS and pretreated with 1% H_2O_2 (vol/vol) in PBS to eliminate endogenous peroxidase activity. Nonspecific antibody binding sites were blocked and tissues were permealized with 2% normal goat serum (NGS, vol/vol) in PBS and 0.3% Triton X-100 (vol/vol). Sections were transferred into a 1:200,000 dilution of a monoclonal mouse antibody to Cre recombinase (α-Cre, Millipore) for 48 h at 4 °C. Immunoreactivity was detected after tissue incubations in biotinylated antibody to mouse (Jackson ImmunoResearch Laboratories; 1:1,000), then in ABC-Elite reagent (Vector Laboratories, 1:1,000 dilutions of solutions A and B in Tris-buffered saline, TBS), for 1 h each. The peroxidase developer contained 0.05% diaminobenzidine (DAB, wt/vol), nickelammonium-sulfate and 0.002% H_2O_2 in TBS. Sections were mounted and cover slipped with DPX Mountant (Electron Microscopy Sciences).

For fluorescence immunocytochemistry, slices were incubated in PBS containing 2% NGS and 0.1% Triton X-100 and one of the following primary antibodies: rabbit antibody to parvalbumin (α-parvalbumin, 1:300, Code, parvalbumin-28; Swant), monoclonal rat antibody to somatostatin (α-SOM, 1:100, Millipore) or α-Cre (1:1,000, Millipore). After several washes, sections were incubated with secondary antibodies: Alexa Fluor 633–conjugated donkey antibody to rabbit (1:200, Invitrogen), DyLight 649–conjugated goat antibody to rat (1:500) or DyLight 488–conjugated goat antibody to mouse (1:300, all from Jackson ImmunoResearch Laboratories). Confocal stack images (25–35 slices, 1-µm optical thickness) from the CA1 region of the hippocampus were acquired (40× objective) using a Leica DM6000 B confocal microscope. The numbers of fluorescent cell bodies were counted on maximum-projected stack confocal images.

Double-labeling for somatostatin and Cre recombinase (**Supplementary Fig. 3c**) was done as follows. First, sections were pretreated with 2% NGS in PBS and 0.3% Triton X-100 followed by incubation in α-SOM (1:100, Millipore) for 48 h at 4 °C. Somatostatin immunoreactivity was detected with DyLight 649–conjugated goat antibody to rat IgG (1:500, Jackson ImmunoResearch Laboratories). Immunolabeled sections were then incubated with antibody to Cre (1:1,000, Millipore) and then with DyLight 488–conjugated goat antibody to mouse.

Analysis of viral labeling efficiency. Following electrophysiological recordings, slices were processed for quantification of viral labeling efficiency. Slices were fixed in 4% paraformaldehyde, washed and re-sectioned (50 µm). Viral labeling efficiency was quantified as the ratio of the density of PSAM[L141F]-GlyR–expressing interneurons in layers of CA1 and the total density interneurons in CA1 layers. For *Gad65-cre* mice, the total density of interneurons was determined in progeny of crosses of *Gad65-cre* with a Cre-dependent tdTomato reporter strain ($n = 15$). For *Som-cre* and *Pvalb-cre* mice, the total densities were obtained from somatostatin ($n = 8$) and parvalbumin ($n = 6$) fluorescence immunocytochemical

staining, respectively. For immunocyochemical characterization, hemizygous (*C57BL/6;Som-cre* and *C57BL/6;Pvalb-cre*) mice were used.

The strong fluorescence signal in ChR2-sfGFP-expressing CA3SCs masked the weak GFP fluorescence of PSAM[L141F]-GlyR–expressing interneurons. To visualize PSAM[L141F]-GlyR+ interneurons during targeted electrophysiological recordings, we injected mice with rAAV(*PSAM[L141F]-GlyR*)[Cre] and rAAV(*tdTomato*)[Cre] (3:1 ratio). The overlap of tdTomato+ cells and PSAM[L141F]-GlyR+ cells was first quantified by performing a *post hoc* immunofluorescence procedure to directly detect the hybrid PSAM[L141F]-GlyR using Alexa 647–conjugated α-bungarotoxin (α-BTX, 1:3,000, Invitrogen), selective for the mutated α7-nAChR receptor binding site of PSAM. The α-BTX staining in PSAM[L141F]-GlyR+ cells could be clearly separated from the weak staining of endogenous α7-nAChRs in the hippocampus. Confocal stack images (25–35 slices, 1-µm optical thickness) were collected from the entire CA1 region, by stitching together multiple stacks made with a 40× objective. Stitched-together stacks covering all of CA1 were collapsed into one *z* plane, and cell bodies that were labeled for tdTomato and/or α-BTX Alexa 647 were counted in each layer (ImageJ, US National Institutes of Health), allowing for quantification of the density and overlap of neuronal expression. We found high degree of overlap between tdTomato and α-BTX signal (percentage of α-BTX in tdTomato in all layers: *Gad65-cre* = $87 \pm 3\%$, $n = 16$; *Som-cre* = $98 \pm 2\%$, $n = 7$; *Pvalb-cre* = $88 \pm 6\%$, $n = 9$; **Supplementary Fig. 2c**). Thus, in subsequent experiments, the expression of tdTomato was routinely used to estimate the density of PSAM[L141F]-GlyR+ cells.

Digital images of α-BTX staining were pseudo-colored to either blue (**Supplementary Fig. 3d**) or black on a white background instead of its dark red native color on a black background (**Supplementary Figs. 2c** and **4a**). Similarly, digital images of tdTomato or GFP staining were sometimes pseudo-colored to black on a white background instead of its red native color on a black background (**Figs. 2e** and **3a,c** and **Supplementary Fig. 3b,e**).

Identification of intracellularly labeled interneurons. Slices containing a biocytin-filled (0.2%) interneuron were fixed, washed, cryo-protected and re-sectioned (50 µm). The endogenous peroxidase activity was then blocked with 1% H_2O_2 in PBS, followed by permealization with TBS and 0.3% Triton X-100. Sections were then incubated in avidin-biotin complex in TBS (1:200; Elite ABC kit, Vector Labs), pre-incubated with 0.05% DAB in Tris buffer, and developed with the addition of H_2O_2. Some recovered neurons were later reconstructed in Neurolucida (MBF Bioscience).

For somatostatin immunocytochemistry on biocytin-filled interneurons ($n = 10$; **Supplementary Fig. 5a**), filled cells were visualized with Alexa 594–conjugated streptavidin (1:1000 or 1:3000, Invitrogen) and somatostatin immunoreactivity was detected with rat antibody to SOM (1:100, Millipore) followed by DyLight 649–conjugated goat antibody to α-rat (1:500). Following immunocytochemical evaluation, the sections were de-mounted and the recorded cells were labeled with avidin-biotin complex as described above.

Multicompartmental model. Simulations were performed using NEURON, with the same CA1 cell geometry and channel conductances as were used in ref. 50. Excitatory conductance-based synapses consisting of AMPA and NMDA components were placed throughout strata oriens and radiatum with a spatial distribution proportional to that measured anatomically[20]. Synapse activation times followed a Poisson process with a rate chosen to produce a somatic current near 450 pA in the absence of inhibition and under somatic voltage clamp. Inhibition was modeled as a constant conductance with a reversal potential of -75 mV and a conductance proportional to the product of the anatomically measured density of inhibitory synapses[20] and the measured firing rate of the relevant interneuron population (perisomatic or dendrite targeting) at the corresponding level of excitatory stimulation (**Supplementary Figs. 3k** and **4g**). Disinhibition was modeled by increasing the conductances of one interneuron population as the antagonistic interneuron population was silenced.

Data analysis. Data was analyzed in Igor Pro 6.04 (Wavemetrics). To produce suprathreshold input-output curves, individual EPSCs with a 74-ms ISI between each point of the photostimulation grid were first summed off-line with a 4-ms ISI and the mean amplitude of the summed current was measured. Firing rate was calculated from the number of action potentials during the 250 ms of phasic photostimulation. Changes in gain for the subthreshold branch

input-output and for suprathreshold input-output curves were calculated as ((control slope – experimental slope)/control slope), where slopes were determined from the peak of the first derivative of the sigmoid fits to the data in the form: base + max/1 + (exp($x$half – x))/rate, where base is the baseline frequency, max is the maximum frequency and rate is the slope parameter. For input-output curves, input shifts (Δoffset) were determined from the $x$half of sigmoid functions. The relative input resistance (R_i) change in somatic and dendritic compartments (**Fig. 5e**,**f** and **Supplementary Fig. 7b**) was calculated by comparing the mean level of hyperpolarization to a current injection (−100 pA) with responses to current injection paired with CA3SCs photostimulation (<100 pA mean input level, responses to synaptic input alone subtracted from paired traces).

Action potentials, if present, were removed by blanking the traces from 2 ms before the action potential's peak to 5 ms after the peak and the traces were subsequently linearly interpolated. Burst duration was calculated by filtering spikes from current-clamp recordings and calculating the full width at half-maximum depolarization across the first 100 ms of CA3SCs photostimulation. Significance was tested with Student's t test or ANOVA with Tukey's significance of difference test for *post hoc*; $P < 0.05$ was considered to be significant. All data are given in mean ± s.e.m. In all figures, symbols with error bars indicate mean ± s.e.m.

50. Poirazi, P., Brannon, T. & Mel, B.W. Arithmetic of subthreshold synaptic summation in a model CA1 pyramidal cell. *Neuron* **37**, 977–987 (2003).

Supplementary Information

Regulation of Neuronal Input Transformations by Tunable Dendritic Inhibition

Matthew Lovett-Barron[1], Gergely F. Turi[1], Patrick Kaifosh[1], Peter H. Lee[2], Frédéric Bolze[3], Xiao-Hua Sun[3], Jean F. Nicoud[3], Boris V. Zemelman[4], Scott M. Sternson[2] & Attila Losonczy[1]

Address:
1) Department of Neuroscience, Columbia University, New York, NY, USA
2) Howard Hughes Medical Institute, Janelia Farm Research Campus, Ashburn, VA, USA
3) Laboratoire de Biophotonique et Pharmacologie UMR 7213 CNRS/UdS, Strasbourg, France.
4) Center for Learning and Memory, University of Texas at Austin, Austin, TX, USA

Supplementary Figures S1 to S9
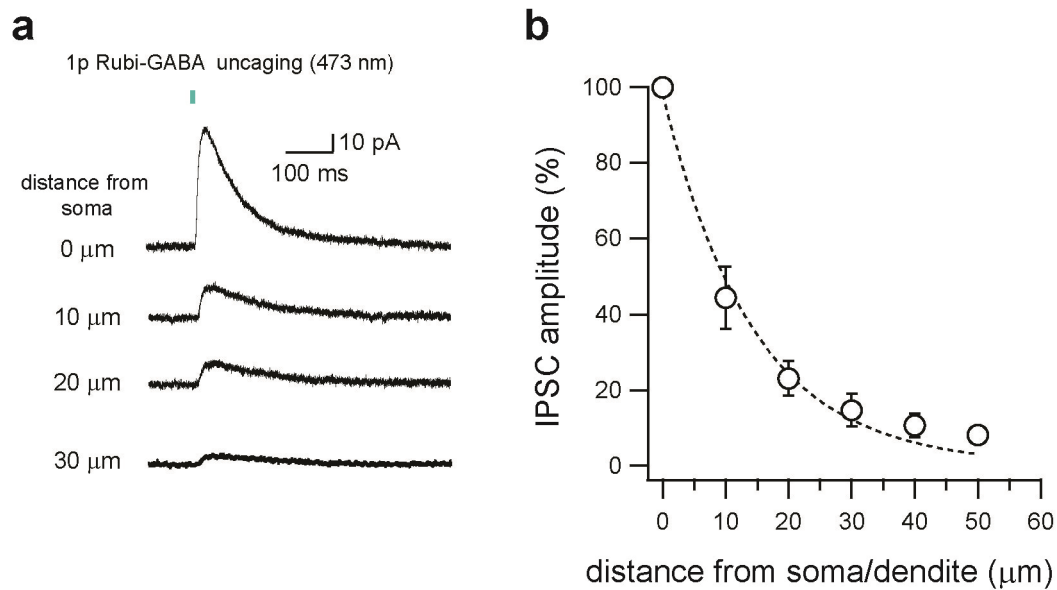
Supplementary Figure 1. Spatial resolution of 1p Rubi-GABA uncaging. (a) Current recorded from a CA1 pyramidal neuron in response to 1p uncaging of Rubi-GABA (80 μM) at various distances from the cell body. **(b)** Summary plot of lateral resolution for 1p GABA uncaging (n = 3). Dotted line is an exponential fit (tau = 14 μm).

2
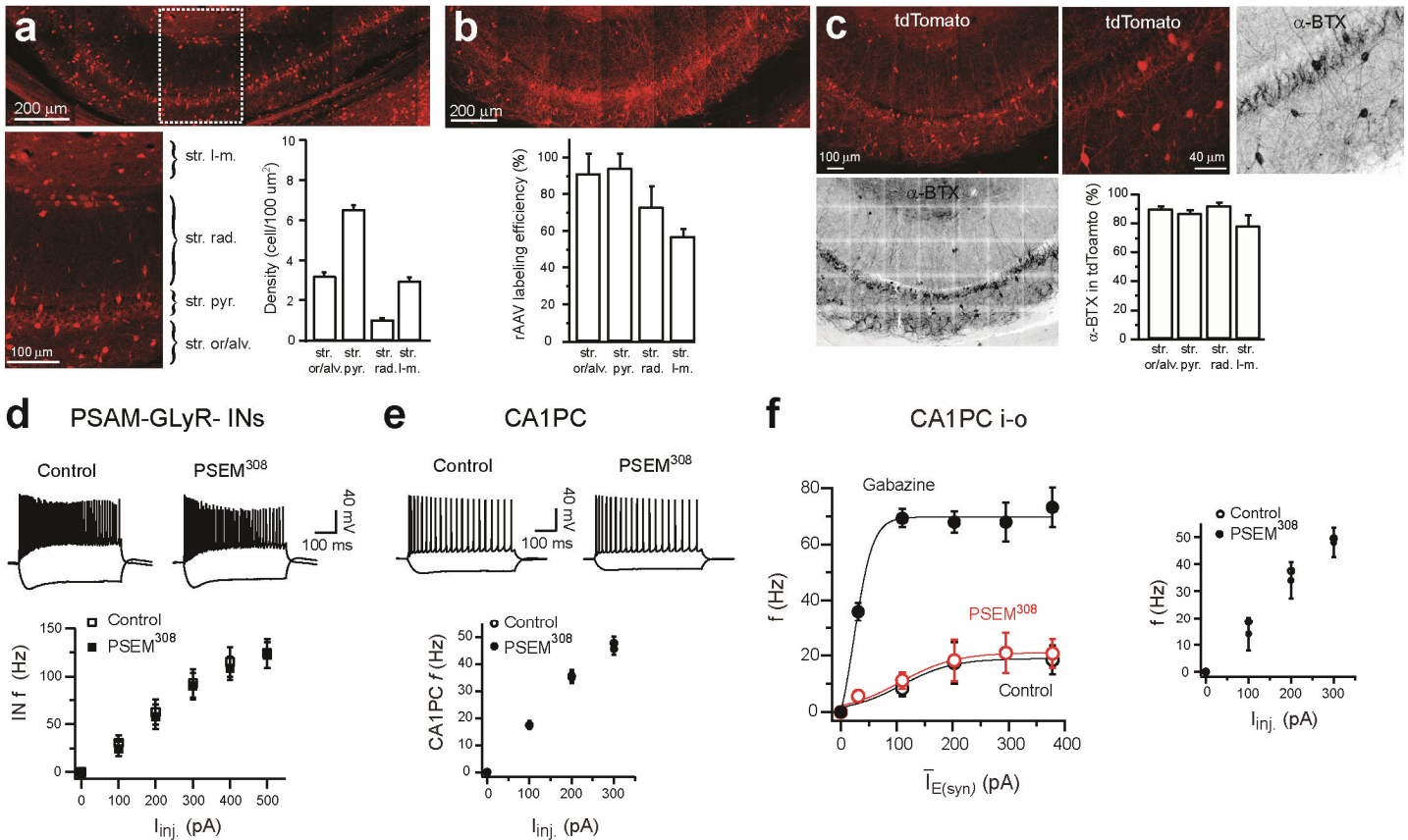
Supplementary Figure 2. Anatomical and physiological characterization of rAAV-mediated PSAM^{L141F}-GlyR expression in *GAD65-Cre* mice. (a) Top: low magnification confocal stack image of tdTomato-expressing interneurons in the CA1 area of the dorsal hippocampus of an offspring of a *GAD65-Cre* and a Cre-dependent tdTomato reporter mouse (*Gt(ROSA)$^{26Sortm9(CAG-tdTomato)Hze}$*). Bottom left: dashed boxed area is expanded to show labeling in various layers of the hippocampal CA1 region. Bottom right: summary bar graph of the density of tdTomato labeled interneurons in the layers of CA1 (n = 16 in n = 8 mice; *str. or./alv.*: strata oriens/alveus, *str. pyr.*: stratum pyramidale, *str. rad.*: stratum radiatum, *str. l-m*: stratum lacunosum-moleculare). **(b)** Top: low magnification confocal stack image of tdTomato-expressing interneurons in the CA1 area of the dorsal hippocampus pf a *GAD65-Cre* mouse injected with a mixture (3:1 ratio) of Cre-dependent rAAV expressing PSAM^{L141F}-GlyR [rAAV(*PSAM^{L141F}-GlyR*)^{Cre}] and tdTomato [rAAV(*tdTomato*)^{Cre}]. Bottom: summary bar graph of rAAV labeling efficiency in layers of the dorsal hippocampal CA1 region in *GAD65-Cre* mice (n = 8 slices in n = 8 mice). **(c)** Top: low-(left) and high-(middle) magnification confocal images of viral tdTomato labeling. Below is the high-magnification image pseudocolored to black on a white backgound. Right: high magnification of alpha-bungarotoxin immunofluorescence (α-BTX) from the CA1 region of the injected hippocampus. Bottom right: summary graph showing the colocalization of α-bungartotoxin and tdTomato labeling in GAD65+ interneurons in layers of the hippocampal CA1 region (n = 16). **(d)** Top: representative voltage traces for somatic depolarizing and hyperpolarizing current injections from PSAM-GlyR-negative interneurons in control and in the presence of 3 μM PSEM^{308}. Bottom: summary of somatic current injection-evoked firing rate for PSAM-GlyR-negative interneurons in control and in the presence of PSEM^{308} (n = 16). **(e)** Top: representative voltage traces for somatic depolarizing and hyperpolarizing current injections in control and in the presence of PSEM^{308} from CA1PCs in slices injected with rAAV(*PSAM^{L141F}-GlyR*)^{Cre} in control and in the presence of PSEM^{308}. Bottom: summary of somatic current injection-evoked firing rate for CA1PCs in control and in the presence of PSEM^{308} (n = 30). **(f)** Left: summary i-o relationship of CA1PCs in response to CA3-SC photostimulation from slices lacking PSAM^{L141F}-GlyR-exression (n = 5) in control, in the presence of PSEM^{308}, and 20μM gabazine. Lines are sigmoidal fit to the data. Right: somatic f-I relationship for CA1PCs from slices lacking PSAM^{L141F}-GlyR in control and in PSEM^{308} (n = 5).

3
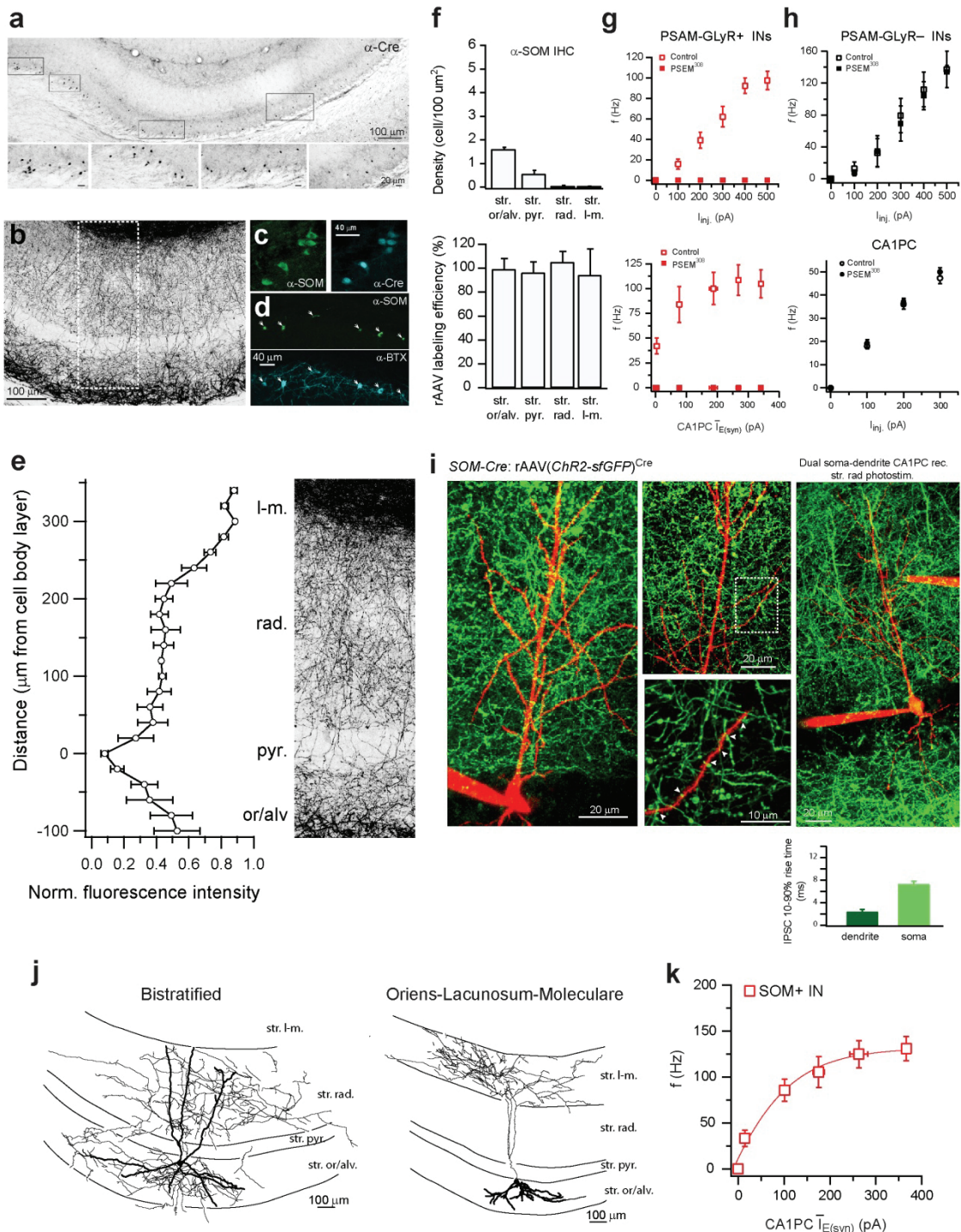
Supplementary Figure 3. Anatomical and physiological characterization of rAAV-mediated PSAM^L141F^-GlyR expression in *SOM-Cre* mice. (a) Low magnification bright-field image of the hippocampal CA1 region with Ni-DAB immunostaining for Cre recombinase. Boxed areas are expanded in insets to show Ni-DAB labeled nuclei in *strata oriens/alveus* and *pyramidale*. **(b)** Low magnification pseudocolored grayscale confocal image stack (20 μm) showing labeling pattern in layers of CA1 in *SOM-Cre* mice injected with rAAV(*sfGFP*)^Cre^. **(c)** Co-localization of somatostatin (α-SOM) and Cre recombinase (α-Cre) in CA1 *stratum oriens/alveus* interneurons in *SOM-Cre* mice. **(d)** Co-localization of somatostatin (α-SOM) and alpha-bungarotoxin (α-BTX) in CA1 *stratum oriens/alveus* interneurons in SOM-cre mice injected with rAAV(*PSAM^L141F^-GlyR*)^Cre^. **(e)** Left: summary plot of normalized fluorescence intensity as a function of distance from the cell body layer (bins: 20 μm) in *SOM-Cre* mice (n = 3) injected with rAAV(sfGFP)^Cre^ into CA1. Hippocampal sections *SOM-Cre* mice virally expressing sfGFP were analyzed to reveal laminar distribution of interneuronal processes.

4

Confocal laser scanning microscope images stacks spanning the entire depth of the CA1 region were taken. Images were rotated to have a vertical axis parallel with the surface of the hippocampus. The position of the pyramidal layer was determined in all images by the experimenter. All images were analyzed semi-automatically in ImageJ. First, background was corrected on 8-bit binary images and average pixel intensity was calculated in 20 x 20 μm areas spanning from *str. oriens/alveus* to *str. lacunosum-moleculare*. Normalized average pixel intensity, triggered by the position of the pyramidal layer, was displayed as a function of the distance from the pyramidal layer center for both lines. Right: expanded boxed area from *b*. **(f)** Top: summary bar graph of the density of SOM+ labeled interneurons in the layers of CA1 area (n = 8, *str. or./alv.: strata oriens/alveus, str. pyr.: stratum pyramidale, str. rad.: stratum radiatum, str. l-m: stratum lacunosum-moleculare*). Bottom: summary of rAAV labeling efficiency in layers of the dorsal hippocampal CA1 region in *SOM-Cre* mice injected with a mixture (3:1 ratio) of Cre-dependent rAAV expressing PSAM[L141F]-GlyR [rAAV(*PSAM[L141F]-GlyR*)[Cre]] and tdTomato [rAAV(*tdTomato*)[Cre]]. **(g)** Top: bath application of 3 μM PSEM[308] completely silences PSAM[L141F]-GlyR+ interneurons to somatic current injection in *SOM-Cre* mice. Bottom: PSEM[308] completely silences PSAM[L141F]-GlyR+ interneurons to CA3-SCs photostimulation in *SOM-Cre* mice (n = 11). **(h)** Top: PSEM[308] application has no effect on f-I curves of PSAM[L141F]-GlyR-negative interneurons (n = 6) in *SOM-Cre* mice. Bottom: PSEM[308] application has no effect on f-I curves of CA1 pyramidal neurons (n = 11) in *SOM-Cre* mice. **(i)** Representative examples of expression pattern in *SOM-Cre* mice. Left: 2-photon image stack of virally labeled interneurons in *SOM-Cre* mice [green; injected with rAAV(*ChR2-sfGFP*)[Cre]] with respect to CA1PC morphology (red, intracellularly filled with Alexa 594). Note the strong viral labeling overlapping with the dendrites in *str. rad.* of CA1PCs, and the absence of viral labeling overlapping with the pyramidal layer. Middle: 2-photon image stack of a different cell, with boxed inset showing multiple putative contacts of SOM+ inhibitory axons with the spiny oblique CA1PC dendrite (arrowheads). Right: Dual recording from the soma and dendrite of a CA1PC in slices expressing ChR2-sfGFP in SOM+ interneurons. Summary graph below shows the shorter rise time for IPSCs recorded in the dendrite versus the soma for SOM+ IN photostimulation (n = 2 dual rec., n = 5 somatic rec.), indicating the dendritic origin of their source. **(j)** Representative examples of reconstructions of the axonal and dendritic arborizations of SOM+ interneurons. Left: interneuron with axonal arborization confined to the proximal dendritic layers of CA1. Right: interneuron with axonal arborization confined to the distal dendritic layer of CA1. Out of the five identified SOM+ interneurons, three INs had axonal arborizations in proximal dendritic layers of CA1, and two were identified as O-LM interneurons with axons confined to the *str. lacunosum-moleculare.* **(k)** I-o function of SOM+ interneurons (n = 8) in response to CA3-SCs ChR2-photostimulation. Interneuron firing rates are plotted as functions of mean excitatory CA3-SCs input obtained from consecutively recorded CA1PCs. Line is a sigmoidal fit.

5
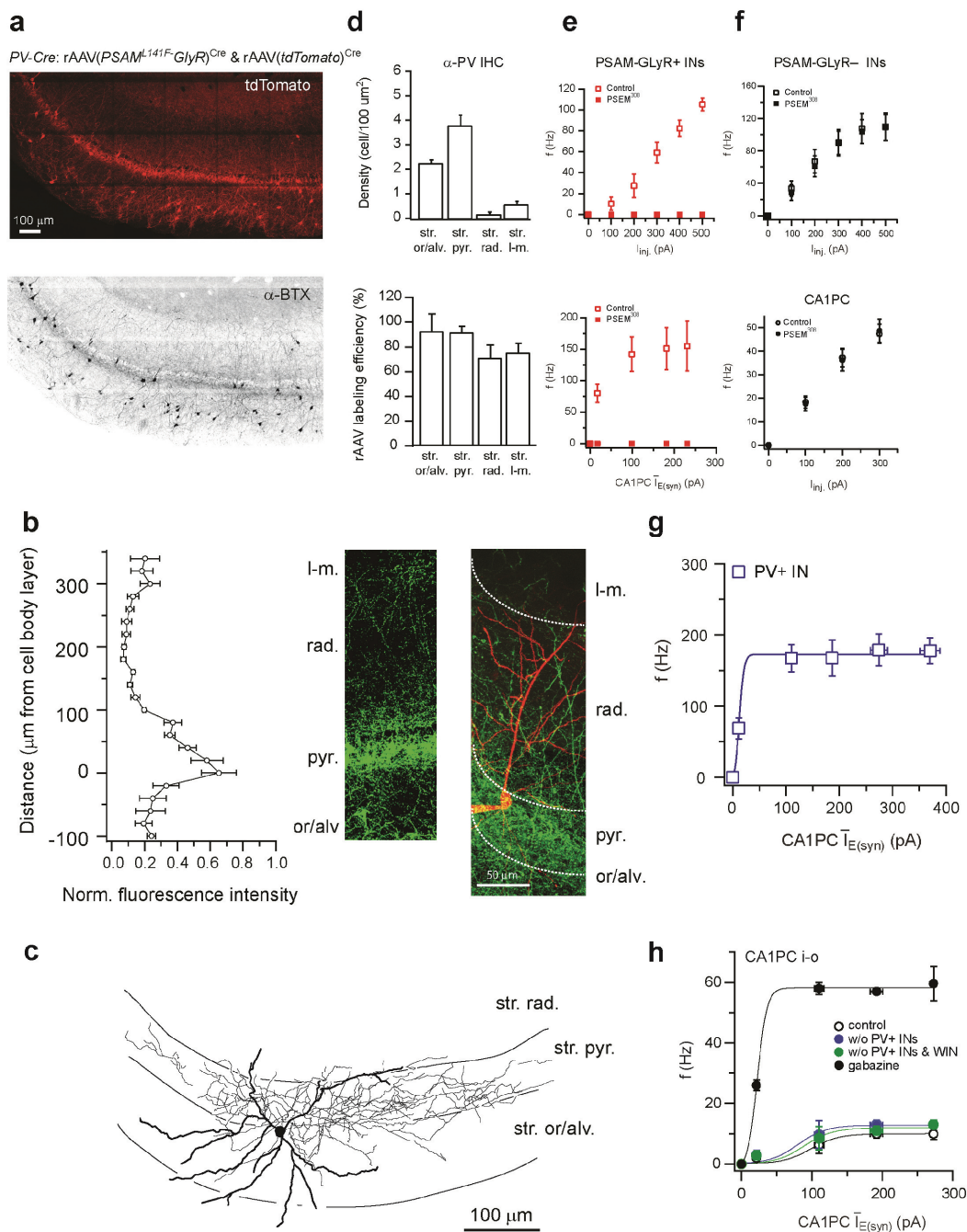
Supplementary Figure 4. Anatomical and physiological characterization of rAAV-mediated PSAM^L141F-GlyR expression in *PV-Cre* mice. (a) Co-localization of virally expressed tdTomato and alpha-bungarotoxin (α-BTX) in sections of CA1 from *PV-Cre* mice injected with rAAV($PSAM^{L141F}$-$GlyR$)^{Cre} and rAAV($tdTomato$)^{Cre}. **(b)** Left: summary plot of normalized fluorescence intensity as a function of distance from the cell body layer (bins: 20 μm) in *PV-Cre* mice (n = 3) injected with rAAV($sfGFP$)^{Cre} into CA1. Middle: example confocal image stack from CA1 area from *PV-Cre* mice injected with rAAV($sfGFP$)^{Cre} into CA1. Right: 2-photon image stack of virally labeled interneurons in *PV-Cre* mice [green; injected with rAAV($ChR2$-$sfGFP$)^{Cre}] with respect to CA1PC morphology (red, intracellularly filled with Alexa 594). Note the strong axonal labeling overlapping with the soma of CA1PCs, and minimal labeling overlapping with the dendritic regions. **(c)** Example of reconstruction of the axonal and dendritic arborizations of a PV+ interneuron showing axon arborization confined to cell body layer of CA1. Two additional identified interneurons had similar axonal arborization. **(d)** Top: summary bar graph of the density of tdTomato-labeled interneurons in the layers of CA1 area (n = 6; *str. or./alv.: strata oriens/alveus, str. pyr.: stratum pyramidale, str. rad.: stratum radiatum, str. l-m: stratum lacunosum-moleculare*). Bottom: summary of rAAV labeling efficiency in layers of the dorsal

6

hippocampal CA1 region in *PV-Cre* mice injected with a mixture (3:1 ratio) of Cre-dependent rAAV expressing PSAM^{L141F}-GlyR [rAAV*(PSAM^{L141F}-GlyR)*^{Cre}] and tdTomato [rAAV*(tdTomato)*^{Cre}]. **(e)** Top: bath application of PSEM^{308} (3 µM) completely silences PSAM^{L141F}-GlyR+ interneurons to somatic current injection in *PV-Cre* mice. Bottom: PSEM^{308} (3 µM) completely silences PSAM^{L141F}-GlyR+ interneurons to CA3-SCs photostimulation in *PV-Cre* mice (n = 5). **(f)** Top: PSEM^{308} application has no effect on f-I curves of PSAM^{L141F}-GlyR-negative interneurons (n = 10) in *PV-Cre* mice. Bottom: PSEM^{308} application has no effect on f-I curves of CA1PCs (n = 12) in *PV-Cre* mice. **(g)** I-o function of PV+ interneurons (n = 11) in response to CA3-SCs ChR2-photostimulation. Interneuron firing rates are plotted as functions of mean excitatory CA3-SC input obtained from consecutively recorded CA1PCs. Line is a sigmoidal fit. **(h)** Summary plot of CA1PC i-o relationships in control conditions, during silencing of PV+ INs, and during subsequent addition of the CB$_1$ receptor agonist WIN-55,212-2 (1 µM) in the presence of PSEM^{308} (n = 7). Note that simultaneous silencing of perisomatic PV+ interneurons combined with reduced GABA release from CCK+ interneurons has no effect on the firing rate of CA1PCs, while subsequent application of gabazine reliably increased CA1PCs firing rate.

7
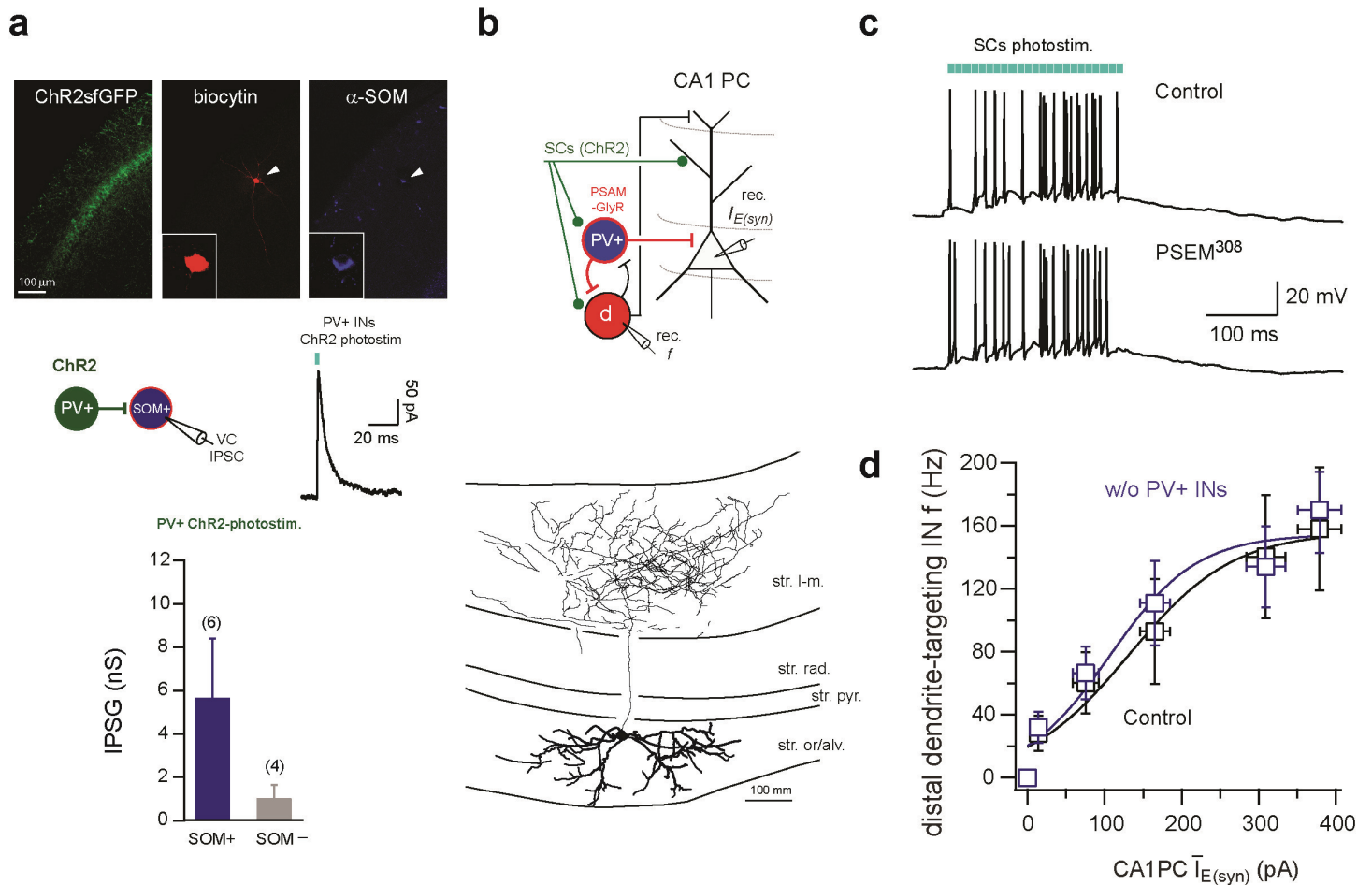
Supplementary Figure 5. Disinhibitory influences of PV+ interneurons on SOM+ interneurons and O-LM cells. (a) Top: Low magnification confocal image stacks of somatostatin-immunopositive interneuron revealed by intracellularly-filled Alexa594 and somatostatin immunofluorescence (pseudocolored to blue) recorded from a CA1 slice with ChR2-sfGFP expression in PV+ interneurons. Enlarged insets showing perinuclear somatostain immunoreactivity at the image plane of the cell body. Middle: Schematic of recording configuration and voltage-clamp trace from SOM+ interneuron receiving a large-amplitude IPSC upon ChR2 photostimulation of PV+ axons (middle) Bottom: summary bar graphs of inhibitory postsynaptic conductances (IPSGs) recorded from all somatostatin immunopositive (SOM+, n = 6 out of n = 10 tested for somatostatin-immunoreactivity, blue) and all somatostatin immunonegative (SOM−, n = 4 out of n = 10 tested for somatostatin-immunoreactivity, grey) interneurons during photostimulation of PV+ interneurons in *PV-Cre* mice injected with rAAV(*ChR2-sfGFP*)^Cre. **(b)** Top: schematic of recording configuration (*d*: dendrite-targeting). Bottom: reconstruction of the axonal and dendritic arborizations of a recorded O-LM interneuron showing axonal arborization confined to the distal dendritic layers of CA1. **(c)** Representative voltage traces from an O-LM interneuron to CA3-SCs photostimulation in control and after silencing PV+ interneurons [rAAV(*PSAM^{L141F}-GlyR*)^Cre and rAAV(*tdTomato*)^Cre injected into CA1 of *PV-Cre* mice] **(d)** Summary of i-o relationship for identified O-LM cells before and after silencing PV+ interneurons (n = 6).
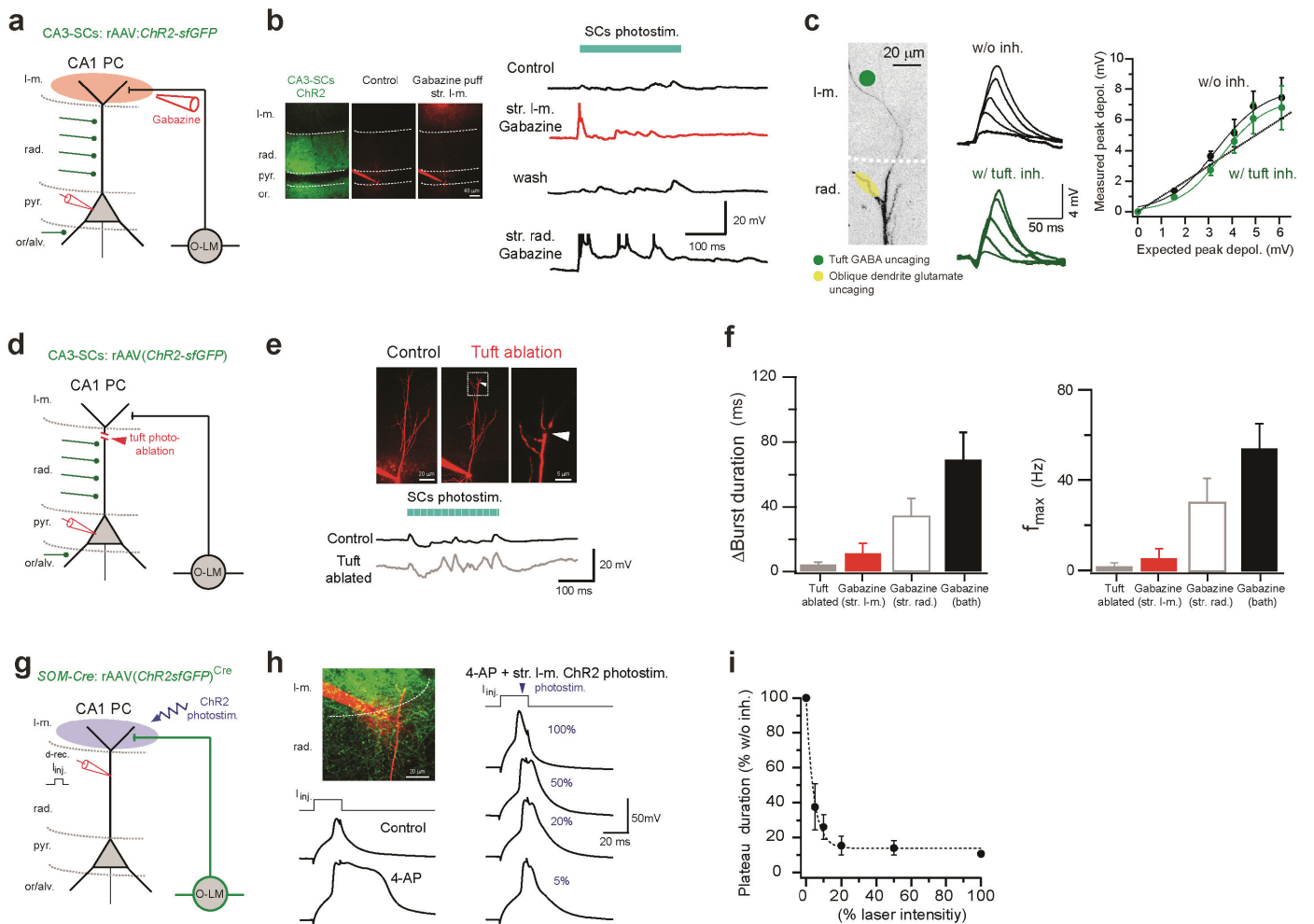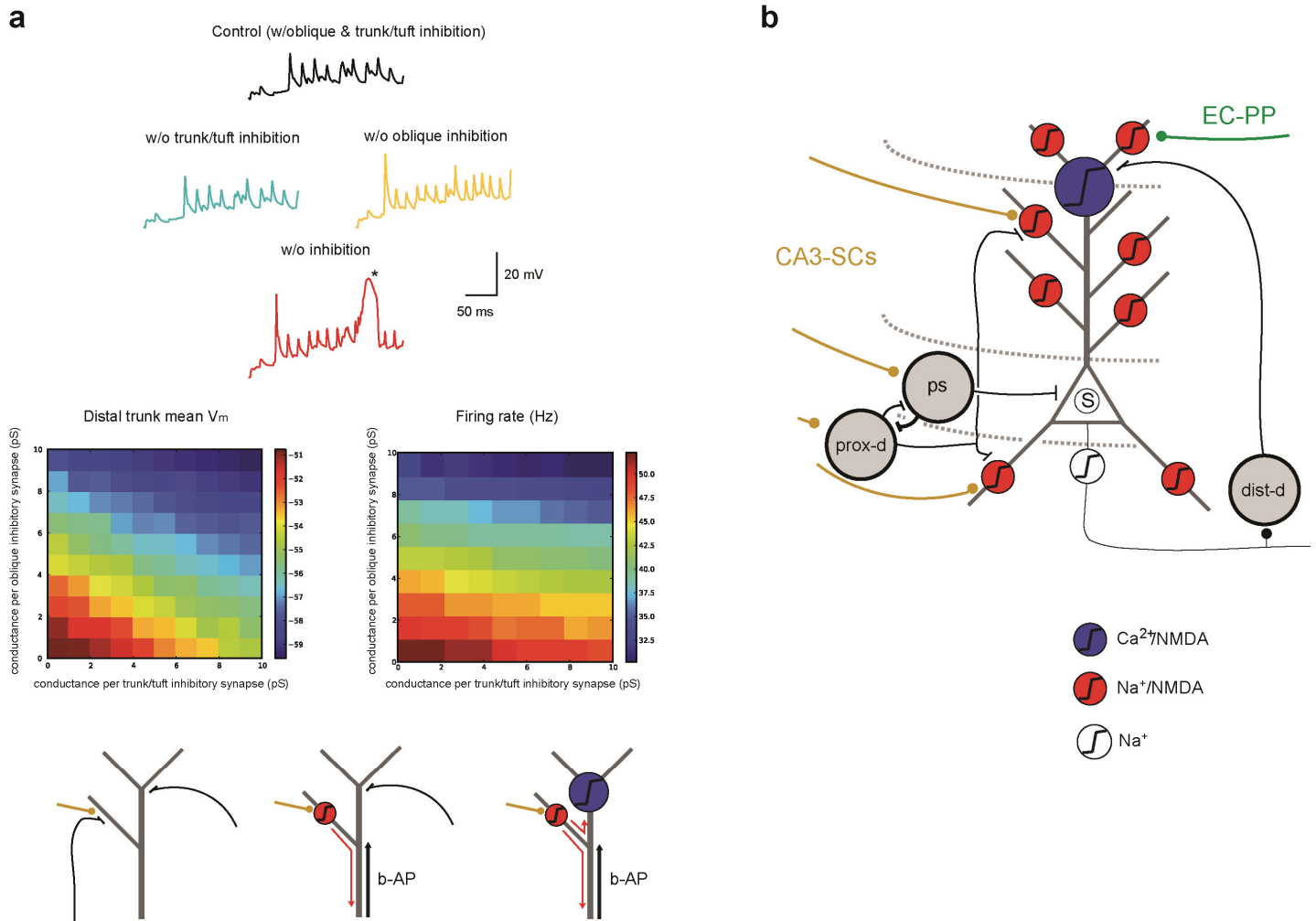
Supplementary Figure 6. Distal inhibition in *stratum lacunosum-moleculare* plays a minor role in CA3-SCs integration in oblique dendrites, but controls global plateau spikes. **(a)** Schematic of recording configuration, in which the responses of a CA1PC are recorded to CA3-SCs photostimulation, with and without local gabazine puff (20 µM) applied to the distal dendritic tuft in *str. lacunosum-moleculare* (focally blocking GABAergic input in the tuft). **(b)** Left: single-plane 2-photon images of intracellularly recorded CA1PC (red) before and after distal gabazine puff (red bolus; Alexa594 included in gabazine puff solution) and geometry with respect to the ChR2-sfGFP+ CA3-SCs (green). Right: responses of CA1PC to CA3-SCs photostimulation in control conditions, (top, black), upon gabazine puff to *str. lacunosum-moleculare* (middle, red), subsequent washout (middle, black), and upon gabazine puff to *str. radiatum* (bottom, black). For focal application of 20 µM gabazine (with 50 µM Alexa 594), a puffer pipette (~2-5 µm tip diameter) was positioned above the tuft region. Duration of gabazine application (10-15 sec) was controlled by a Picospritzer. The spatial extent of the Alexa 594 signal was used the estimate the spread of gabazine application in the tissue. **(c)** Left: single-plane 2-photon image of distal dendrites of recorded hippocampal CA1PC (filled with Alexa 594, grey pseudocolored) and locations of two-photon glutamate uncaging (yellow dot) in distal *str. radiatum* and one-photon GABA uncaging at tuft region in *str. lacunosum-moleculare* (green dot). Middle: somatic membrane potential responses to increasing number of stimulated oblique synapses in the control case without inhibition (black) and in the presence of tuft inhibition (green). Right: population summary of single-oblique branch i-o function in control and in the presence of tuft inhibition (n = 6). Note that distal tuft inhibition has a negligible effect of oblique EPSP summation. **(d)** Schematic of recording configuration, in which the responses of a CA1PC are recorded to CA3-SCs photostimulation, with and without the presence of an apical tuft.

(e) Top: 2-photon image stack of patch-clamped CA1PC, before and after 2-photon photo-ablation of the distal tuft dendrites at the border of *str. radiatum* and *str. lacunosum-moleculare*, and expanded boxed inset (arrowhead denotes location of 2-photon ablation). Bottom: responses of CA1PC to CA3-SCs photostimulation in control conditions (black) and upon ablation of the tuft (grey). CA1PCs with intact apical dendrites and prominent dendritic tufts were used, confirmed on the two-photon image stacks of the recorded neurons collected at the end of the experiments. Repeated two-photon line scans (200-300 lines, 820 nm, 20 mW) with slow pixel dwell times (40-60 μs/pixel) were used to photo-ablate apical distal apical trunk at the border of *str. radiatum* and *str. lacunosum-moleculare*. Successful photo-ablation produced an apparent gap on the distal dendrite and removed the prominent sag from voltage responses evoked by hyperpolarizing somatic current injections (data not shown). **(f)** Left: population summary data showing the maximum change in burst duration from control conditions after tuft ablation (n = 5), or puffing gabazine to *str. lacunosum-moleculare* (n = 4) or *radiatum* (n = 4), compared to bath application of gabazine (n = 8), which completely blocks inhibition in the slice. Right: summary graph of maximum firing rate upon tuft ablation and upon local or bath application of gabazine. **(g)** Schematic of recording configuration in which CA1PCs are patched at the distal apical dendrite, and inhibition is delivered via focal photostimulation of ChR2+ axons from SOM+ O-LM cells in *str. lacunosum-moleculare*, which synapse on distal apical tuft dendrites. **(h)** Top left: high-magnification 2-photon image stack of intracellular recording from the distal apical dendrite of a CA1PC (red) and ChR2-sfGFP+ axons from SOM+ O-LM cells. Recordings are performed in acute slices from *SOM-Cre* mice injected with rAAV($ChR2\text{-}sfGFP$)^{Cre} into dorsal CA1. Bottom left: V_m responses recorded from distal dendrite to brief current injection (+400pA, 20ms) in control conditions, and upon blockade of K^+ channels with bath application of 4-AP (2 mM). Partial blockade of A-type K^+ channels turn the dendritic response to current injection into a long-lasting dendritic plateau. Right: V_m responses to dendritic current injection in the presence of 4-AP, paired with ChR2-photostimulation of *str. lacunosum-moleculare* at various laser intensities (blue). **(i)** Population summary data (n = 3) showing the effect of distal O-LM inhibition on the duration of dendritic plateau potentials evoked by dendritic current injection in the presence of 4-AP. Note that even low levels of ChR2-photostimulation in *str. lacunosum-moleculare* successfully blocked the prolonged dendritic plateaus that are present in the absence of evoked inhibition.
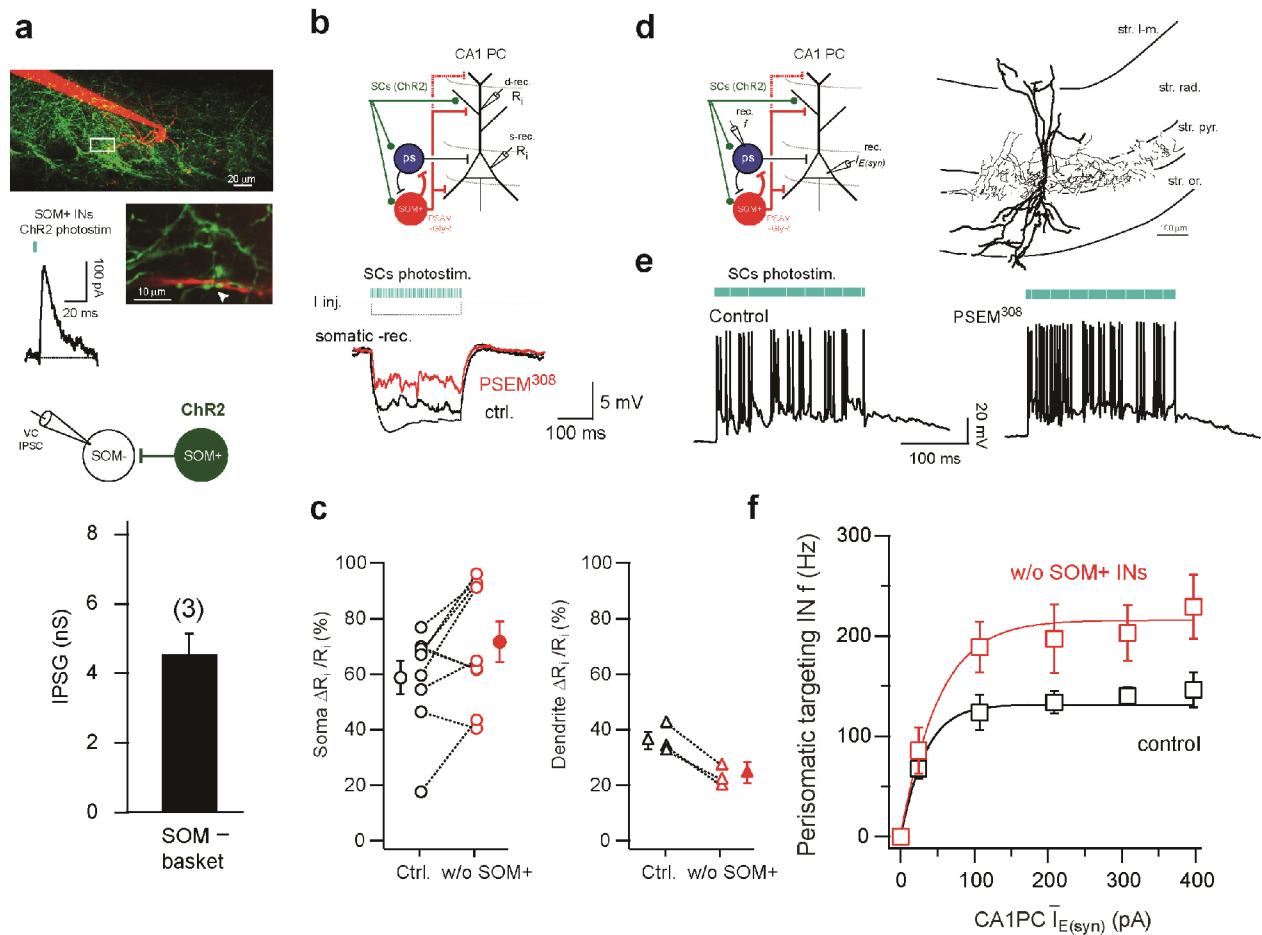
Supplementary Figure 7. Disinhibition of perisomatic-targeting interneurons during silencing of SOM+ interneurons, and resulting conductance changes in CA1PCs. (a) Top: 2-photon image stack of intracellularly recorded SOM– IN (Alexa 594, red) in CA1 slice expressing ChR2-sfGFP in SOM+ INs (green), with boxed inset showing putative axodendritic contact (arrowhead). Voltage-clamp recording shows ChR2 photostimulation-evoked IPSC recorded in SOM– IN. Middle: recording configuration. Bottom: summary of mean conductance recorded from identified perisomatic-targeting interneurons (black, SOM–, n = 3) during SOM+ INs photostimulation in *SOM-Cre* mice injected with rAAV(*ChR2-sfGFP*)[Cre]. **(b)** Top: schematic of recording configuration (*ps*: perisomatic targeting). Bottom: example voltage traces from somatic whole-cell recordings from a CA1PC in control and after silencing SOM+ INs, showing an increase in perisomatic conductance. **(c)** Summary of changes to dendritic and somatic input resistance induced by synaptic conductance in control and after silencing SOM+ INs. **(d)** Left: schematic of recording configuration. Right: reconstruction of the axonal and dendritic arborizations of the recorded SOM– basket cell showing axonal arborization confined to the cell body layer of CA1. **(e)** Representative voltage traces of recordings from a SOM– basket cell during CA3-SC photostimulation in control and after silencing SOM+ INs [rAAV(*PSAM*^{L141F}-*GlyR*)[Cre] and rAAV(*tdTomato*)[Cre] injected into CA1 of *SOM-Cre* mice] **(f)** Summary of i-o relationship for of identified SOM– perisomatic targeting interneurons before and after silencing SOM+ interneurons (n = 5).

Supplementary Figure 8. Nonlinear integration scheme for CA1 pyramidal cells receiving excitatory and inhibitory inputs. (a) Dissection of the roles of inhibition targeting the apical oblique and apical trunk/tuft CA1PC dendrites in the multicompartmental model. Top: examples of sample voltage traces recorded from the distal trunk in the presence of fixed excitatory input in *stratum radiatum* and different configurations of inhibitory input. The asterisk indicates a slow dendritic spike occurring when inhibition to both oblique and trunk/tuft dendrites was silenced. Middle: inhibition to the apical oblique branches attenuated both distal trunk voltage and mean firing rate more strongly than inhibition to the apical trunk/tuft. Bottom: these results are consistent with the following integration scheme. Removal of co-aligned inhibition to oblique dendrites permits nonlinear synaptic integration of excitatory inputs within single branches, strongly affecting CA1PC firing rate. When inhibition to the trunk and tuft is also removed, excitation, together with enhanced spike backpropagation (*b-AP*) can recruit global dendritic Ca^{2+} spikes to further enhance firing rates**.** When modeling the effects of apical trunk, tuft, and oblique inhibition, inhibitory conductances were restricted to these regions and scaled in terms of conductance per synapse, using the anatomically measured synapse densities. Excitatory synapses were restricted to the apical dendrites in *stratum radiatum* and produced a somatic input current of approximately 350 pA under somatic voltage clamp. All simulations were repeated with 10 different random seeds that determined the placement and activation timing of excitatory synapses. **(b)** Conceptual model of multimodal dendritic computations in CA1 pyramidal cells. Interneurons targeting small diameter dendrites receiving CA3-SCs input (*prox-d,* bistratified interneurons are shown) regulate branch-specific Na^+/NMDA spike generation. Reduced inhibition in thin dendrites leads to local Na^+/NMDA spike generation and burst spiking at the soma. Further suppression of inhibition onto thin dendrites and onto the apical trunk allows local branch nonlinearities to recruit global Ca^{2+}/NMDA plateaus spikes in the distal apical trunk and the apical tuft. Inhibition targeting the dendritic tuft (*dist-d*, oriens-lacunosum-moleculare interneurons are shown) regulate Ca^{2+}/NMDA plateau spike generation in the tuft and excitatory interaction between CA3-SCs and perforant path inputs (EC-PP). Functionally asymmetric disinhibition from perisomatic (*ps*)- to dendrite (*prox-d*)- targeting interneurons compensate for the removal of perisomatic inhibition during rate-coded input output transformations.
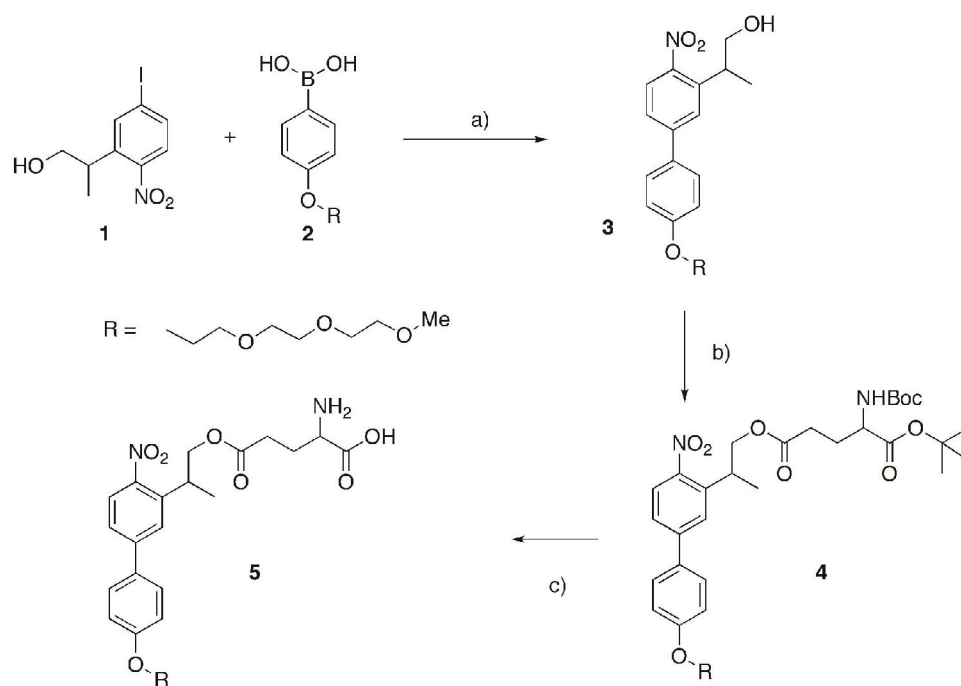
Supplementary Figure 9. Preparation of caged glutamate PENB-L-Glutamate. *a*) Toluene, Pd(PPh$_3$)$_4$, Na$_2$CO$_3$, EtOH, reflux 24 h. *b*) CH$_2$Cl$_2$, DMAP, Boc-L-glutamic acid 1-tert-butyl ester, DCC, room temperature under N$_2$ in the dark, 12 h *c*) CH$_2$Cl$_2$, TFA , room temperature in the dark, 12 h. The cage 3-(2-propyl-1-ol)-4'-tris-ethoxy(methoxy)-4-nitrobiphenyl (PENBOH, *3*) was prepared from 2-(5-iodo-2-nitrophenyl)propan-1-ol (*1*) and 4-*tris*-ethoxy(methoxy) phenylboronic acid (2). DMAP (6 mg, 0.05 mM) was added to a solution of *3* (0.22 g, 0.52 mM) in dichloromethane (10 ml). The mixture was stirred at 0°C for 10 min then Boc-L-glutamic acid 1-tert-butyl ester (0.17 g, 0.57 mmol) and DCC (0.12 g, 0.57 mM) were added quickly. The mixture was stirred at room temperature under N$_2$ for 12 h then evaporated. The residue was purified by column chromatography using gradient elution method of ethyle acetate and petroleum ether afforded a green gel. This last compound (0.25 g, 0.35 mM) was then dissolved in dichloromethane (20 ml), TFA (5 ml) was added and the solution was stirred in dark for 12 h. The solvent was evaporated, the residue was dissolved in dichloromethane (5 ml), precipitated by petroleum ether, washed by diethyl ether and dried in vacuum to afford PENB-L-Glutamate as a yellow powder (0.16 g, 80 % yield). ^{1}H RMN (DMSO-D6) : 7.79 (d, 1H), 7.64 (m, 4H), 7.00 (m, 2H), 4.25 (m, 4H), 3.85 (m, 1H), 3.70 (m, 8H), 3.50 (m, 3H), 2.55 (br, 2H), 2.07 (m, 2H), 1.30 (m, 3H). ^{13}C RMN (DMSO-D6) : 173.46, 160.33, 149.66, 145.90, 138.81, 132.07, 129.53, 126.97, 126.30, 125.83, 116.05, 72.30, 71.24, 70.76, 70.51, 70.39, 69.51, 68.57, 59.19, 55.20, 53.84, 34.10, 30.45, 25.81, 17.90. HRMS :calc. m/z for C$_{27}$H$_{37}$N$_2$O$_{10}$ 549.2448, found 549.2482. The one-photon absorption maximum is located at 317 nm, with an *e* of 9 900 M^{-1}cm^{-1}. The uncaging quantum yield is 0.1 with 90 % glutamate release. The two-photon absorption action cross-sections are 0.45 and 3.3 GM at 800 and 740 nm respectively.

13